

Efficient Numerical Quantification of Flettner Rotor Installations

Niklas Kühl¹

¹Hamburg Ship Model Basin, Bramfelder Strasse 164, D-22305 Hamburg, Germany

May 9, 2025

Abstract

This paper introduces an inviscid Computational Fluid Dynamics (CFD) approach for the rapid aerodynamic assessment of Flettner rotor systems on ships. The method relies on the Eulerian flow equations, approximated utilizing a state-of-the-art Finite Volume Method with a dynamic momentum source term to enforce rotor circulation. The method offers substantial computational savings by avoiding near-wall refinement and easing time step constraints, making it ideal for early design phases such as design space exploration. Validation against potential flow theory and viscous reference simulations confirms that the method reliably predicts lift-induced forces despite its limitations in capturing parasitic drag. Three-dimensional simulations, including idealized wind tunnel setups and full-scale ship applications at high Reynolds numbers (up to $Re_L = 10^8$), demonstrate that results based on low-order convection featuring a solid numerical viscosity yield deviations with respect to viscous reference data of around $\mathcal{O}(10\%)$. Accepting this reasonable loss of predictive accuracy provides a simulation framework with response times in the order of minutes compared to hours or even days.

Keywords: Computational Fluid Dynamics, Modeling & Simulation, Flettner Rotor, Ship Aerodynamics

1 Introduction

The need for sustainable shipping has become much more important in recent years as the maritime industry strives to reduce greenhouse gas emissions and improve the efficiency of ships. One promising approach is utilizing Wind Assisted Propulsion (WASP). In this context, Flettner rotors are a prominent and highly actual example, which technology dates back roughly one century (Greenspan (1969); Seifert (2012)), but is experiencing a renaissance in the modern shipping industry due to new environmental regulations and technological advances. Flettner rotors offer a promising opportunity to utilize their aerodynamic lift, thereby ultimately supporting a ship's propulsion to reduce its overall fuel consumption. Therefore, studying the aerodynamics and flow conditions around these rotors is crucial to optimize their performance.

The fluid dynamic design and optimization of shipbuilding components (e.g., hull, rudder, propulsion unit) involve fluid-physical processes on different spatial and temporal scales. Simultaneous consideration of all systems (e.g., resistance and propulsion or sea-keeping and maneuverability) is challenging, so a sequential approach is usually pursued instead. Especially in early design phases, tools with short response times are utilized, and a reduced prediction quality due to their model simplifications is accepted. In this context, inviscid Computational Fluid Dynamics (CFD) methods are often used, which provide a reasonable compromise between quality of solution and time to solution (John and Anderson (1995); Ferziger and Peric (2012)). More complex calculations are carried out in a later design phase. A classic example refers to the hydrodynamic ship-line design, which explores a comparatively large design space in the initial design stage with the help of low-effort flow-potential-based wave resistance approaches. More sophisticated, viscous prediction methods are only applied to selected, pre-optimized design configurations. The outlined process chain may differ slightly from case to case, but it is a common industrial practice in hydrodynamic design.

Driven by the desire to reduce ship emissions, the demand for WASP is increasing. The increased fuel saving through, e.g., Flettner rotors, poses new challenges for the design process. At the same time, a further component must be considered, that interacts with the ship's superstructure and must be suitably optimized. In order to realistically evaluate the performance of Flettner rotors, precise CFD analyses are required, that should follow at least a statistical descriptions of flow turbulence, cf. International Towing Tank Conference (2021), or Menter (1994); Samareh (1999). In practice, mainly non-zonal hybrid filtered/averaged methods

to model flow turbulence have been established, which, however, are associated with a considerable numerical effort (Menter (2009); Spalart et al. (1997)).

Recent investigations have focused on validating CFD models for Flettner rotors under varying operational parameters, including spin ratios and turbulence models, demonstrating solid agreement with experimental benchmarks, e.g., De Marco et al. (2014, 2015); Bordogna (2020). Further research has examined the influence of rotor geometry and flow conditions on lift generation and drag characteristics using high-fidelity CFD approaches, cf. Kwon et al. (2022); Huang et al. (2023); Arief et al. (2018).

This manuscript aims to evaluate the effectiveness and potential benefits of Flettner rotors on ships in an initial design stage using inviscid Eulerian CFD strategies. The presented method utilizes a volume force approach to realistically adjust the fluid circulation generated by the Flettner rotor. The presented method follows a classical, incompressible Finite-Volume-Method with co-located variable arrangement. The main difference to viscid approaches refers to the adaptation of wall boundary conditions from no-slip to slip treatment. In addition to a reduced number of transport equations, the approach allows for significantly coarser temporal and spatial discretization efforts, especially in the near-wall region, resulting in reduced numerical efforts. The necessary rotor circulation is adjusted by a suitable volume force model in rotor adjacent volumes/cells/elements, whereby the force magnitude is adaptively adjusted during runtime to arrive at a prescribed rotor rotation rate. In order to approximate flow fields governing the above equations for various rotor configurations, we aim at an evaluation procedure that minimizes software interfaces (e.g., different geometry and meshing engines) and re-uses as many routines of the actual CFD code as possible.

The proposed strategy requires an interface to the simulation software in order to prescribe momentum sources, e.g., via suitable user coding. As a result, the methodology can be simply transferred to various CFD solver's. Due to the straight forward body force based rotor model control, the method is highly automat able, especially due to the simple geometry parameterization of Flettner rotors in combination with external grid generators and the consideration of the entire relative wind spectrum ranging from $0^\circ \leq \alpha < 360^\circ$. Hence, the approach allows the systematic investigation of general Flettner rotor configurations, ranging from different dimensions (aspect ratio, end plate to rotor diameter) over position to interaction aspects.

The structure of the manuscript is as follows. The upcoming Sec. 2 gives an overview of the basic model equations, the discrete approximation, and the volume force model. In Sec. 3, the method is verified using academic 2D investigations on a rotating circular cylinder and validated against viscous investigations on two further 3D investigations on an idealized rotor and a rotor ship. Section 4 applies the presented method to the configuration optimization of Flettner rotors on a bulk carrier before the manuscript ends with a summary and outlook in Sec. 5. The paper defines vectors and tensors concerning a spatially fixed orthogonal coordinate system, applying Einstein's summation convention to doubly occurring Latin indices.

2 Aerodynamic Modeling & Simulation Approach

2.1 Continuous Modeling

In a conventional inviscid framework, the following set of equations refer to the local balance of mass as well as linear momentum and governs the temporal (t) evolution of an incompressible fluid's (ρ) velocity v_i and pressure p , viz.

$$\frac{\partial v_k}{\partial x_k} = 0 \quad \text{in} \quad \Omega, \quad (1)$$

$$\frac{\partial \rho v_i}{\partial t} + \frac{\partial v_k \rho v_i}{\partial x_k} + \frac{\partial p}{\partial x_i} - b_i = 0 \quad \text{in} \quad \Omega, \quad (2)$$

where b_i refers to a generic body force. Boundary conditions are based on a numerical wind tunnel in which the ship model to be investigated is placed in the center and separated on the waterline by a symmetry plane Γ^{symm} . In contrast to viscous investigations, a slip wall boundary condition is assumed along the ship's superstructure Γ^{wall} , which suppresses the tangential momentum transport and allows for normal, pressure-induced stresses only. As a consequence, the paper's wall and symmetry boundary condition formally coincide. The true wind is prescribed along the outer horizontal Γ^{horizon} boundaries and ambient pressure values are enforced at the

domain's upper end Γ^{top} . The boundary conditions are briefly noted below:

$$\frac{\partial p}{\partial n} = 0, \quad v_i n_i = 0, \quad \frac{\partial v_i}{\partial n} t_i = 0 \quad \text{on} \quad \Gamma^{\text{wall \& symm}}, \quad (3)$$

$$\frac{\partial p}{\partial n} = 0, \quad v_i = v_i^{\text{true wind}} \quad \text{on} \quad \Gamma^{\text{horizon}}, \quad (4)$$

$$p = p^{\text{ambient}}, \quad \frac{\partial v_i}{\partial n} = 0 \quad \text{on} \quad \Gamma^{\text{top}}. \quad (5)$$

Initial conditions follow a constant true-wind and ambient pressure field, i.e.,

$$v_i = v_i^{\text{true wind}}, \quad p = p^{\text{ambient}} \quad \text{at} \quad t = 0. \quad (6)$$

The fundamental modeling idea assumes that the frictionless method should be able to predict lift effects satisfactorily. The method should provide a solid possibility for reasonably fast predictions and estimations of different Flettner rotor configurations. Due to the neglected viscous effects, drag effects should only be insufficiently represented. However, the paper's investigations are carried out on full-scale ships, so the underlying Reynolds numbers are comparatively large in the order of $\text{Re}_L = \mathcal{O}(10^8)$.

The frictionless process only allows a normal, pressure-based momentum transfer between the wall and the fluid, not a tangential, friction-based companion. This poses a challenge to couple the rotor's rotation with the fluid motion, thus ensuring correct fluid circulation in the rotor's vicinity. However, for given rotor speed N^{rotor} and geometry (surface coordinates x_i^{rotor} and normal vectors n_i^{rotor} as well as center position o_i and the rotation vector, e.g., $\omega_i = 2\pi N^{\text{rotor}} \delta_{i3}$) data, the latter is known a priori, i.e.,

$$\Gamma^{\text{rotor}} = \int v_i t_i d\Gamma^{\text{rotor}} \quad \text{with} \quad \underline{v} = \underline{\omega}^{\text{rotor}} \times (\underline{x} - \underline{o})^{\text{rotor}}, \quad \underline{t} = \underline{n}^{\text{rotor}} \times \underline{e}_3 \quad (7)$$

where $v_i t_i$ refers to the rotor's circumferential velocity component. The example assumes a rotor axis aligned with the third \underline{e}_3 spatial direction. Our approach aims at an equal rotor wall-adjacent fluid velocity, i.e., $v_i^{\text{fluid}} \rightarrow v_i^{\text{rotor}}$. The fluid motion is triggered by an appropriate body force aligned with the rotor's circumferential motion, i.e., $b_i^{\text{fluid}} \propto v_i^{\text{rotor}}$. However, we opt for an integral equivalence based on the fluid's circulation instead of striving for a local equivalence that might require volatile body force with pronounced gradients in both circumferential and radial directions. Hence, we iteratively measure the wall-adjacent fluid circulation and utilize the wall-adjacent body force to drive $\Gamma^{\text{fluid}} = \Gamma^{\text{actual}} \rightarrow \Gamma^{\text{target}} = \Gamma^{\text{rotor}}$. Section 2.3 provides detailed algorithmic aspects regarding this approach, which is fully externally/isolated controllable as long as the flow solver provides a body-force interface – which is usually the case.

2.2 Discrete Treatment

The balance Eqns. (1)-(2) are approximated with the flux-based implicit Finite-Volume-Method FreSCo^+ based on a collocated variable arrangement, cf. Rung et al. (2009); Stück (2012); Kühl (2021). A discrete system of equations of size $NP \times NP$ is formulated to solve for the cell-centered flow field variables. This is achieved through an outer fix-point iteration loop indexed by M at a time step T . Each equation corresponds to the balance of a particular control volume P and is used to compute the cell-centered flow variables, i.e., $[v_i, p]^{\text{P}, T, M}$. Local approximations are constructed from values sampled at the cell center $P \in [1, NP]$ as well as the face centers F that separate the control volume around P from its neighboring volumes.

The system of equations for the outer iteration M is solved using the Portable, Extensible Toolkit for Scientific Computation (PetSC, cf. Balay et al. (2019)), whereby Conjugate Gradient (CG) and BI-Conjugate Gradient (BICG) approaches with Jacobi preconditioning are utilized for the pressure and momentum equations, respectively. Both inner and outer convergence criteria are around $\mathcal{O}(10^{-2})$.

We aim at a numerical process that (a) introduces as little numerical viscosity as possible while at the same time (b) being numerically robust, allowing for rapid inviscid flow predictions. Temporal changes follow an implicit first-order (backward) Euler approximation, and the rotor's circulation-adjusting body force is approximated as a cell-centered momentum source. The latter is incorporated in the pressure-velocity coupling in line with an appropriate momentum-weighted or enhanced Rhie-Chow interpolation scheme, cf. Kühl and Rung (2022). Spatial gradients are consistently approximated via the Gauss divergence theorem. The most delicate part refers to the approximation of convective fluxes, i.e.,

$$\int \frac{\partial}{\partial x_k} \left[\frac{\partial \rho v_k v_i}{\partial x_k} \right] d\Omega \approx \sum_{F(P)} [\rho v_k v_i \Delta \Gamma_k]^{\text{F}, T, M} = [\dot{m} v_i]^{\text{F}, T, M} \quad (8)$$

Two concepts that interpolate the velocity vector v_i^F to the face are considered in this paper: A (a) flux-blending and (b) total variation diminishing (TVD) κ -scheme. The former blends the momentum flux through a cell's face between Upwind Differencing (UD) and Central Differencing (CD), i.e.,

$$v_i^F = \beta v_i^{F,UD} + (1 - \beta) v_i^{F,CD}, \quad (9)$$

thus allowing for a user-defined control of the UD amount that introduces stabilizing but partly unwanted numerical diffusion. The κ -scheme refers to a generalized implementation of van Leer's (Van Leer (1979)) Monotonic Upstream Scheme for Conservation Laws (MUSCL) scheme as a combination of first-order upstream and higher-order approximations characterized by the parameter κ . A damping function ψ dynamically limits local gradients and thus decreasing the approximation order and the implementation reads

$$v_i^F = v_i^U + \frac{1}{2} (v_i^D - v_i^U) \left[\frac{1 + \kappa}{2} \psi(r) + \frac{1 - \kappa}{2} r \psi\left(\frac{1}{r}\right) \right] \quad \text{with} \quad r = \frac{v_i^U - v_i^{UU}}{v_i^D - v_i^U}, \quad \psi(r) = \min\text{mod}(1, \omega_2 r), \quad (10)$$

$$\text{and} \quad r \psi\left(\frac{1}{r}\right) = \min\text{mod}(r, \omega_1) \quad (11)$$

where v_i^D , v_i^U , and v_i^{UU} denote the face's downwind and two upwind values, respectively. The minmod operator is defined as $\min\text{mod}(x, \omega y) = \text{sgn}(x) \max(0, \min(|x|, \omega y \text{sgn}(a)))$ and the two additional argument values read $\omega_1 = \max(1, (9(3 - \kappa))/(10(1 - \kappa)))$ and $\omega_2 = \max(1, (9(3 + \kappa))/(10(1 + \kappa)))$. The formulation allows for mixing between centralized and upwind biased strategies, e.g., CD and the Quadratic Upstream Interpolation for Convective Kinematics (QUICK) via $0.5 \leq \kappa \leq 1.0$, e.g., $v_i^F = v_i^{F,CD}$ for $\kappa = 1$ or $v_i^F = v_i^{F,QUICK}$ for $\kappa = 0.5$. Further details on the implementation can be found in Stück (2012); Manzke (2018).

The considered numerical approaches refer to standard approximation strategies in prominent CFD packages, allowing the transfer of this paper's approaches. Further details on the numerical infrastructure including solver validation or possibilities for design optimization can be found, e.g., Kühl et al. (2021b,a); Loft et al. (2023) or Müller et al. (2021); Kühl et al. (2022); Radtke et al. (2023).

2.3 Rotor Circulation Approximation via Wall-Adjacent Momentum Sources

The relevant algorithmic relationships are outlined below. Algorithm 1 essentially controls the time integration and declares the globally required variables needed in the later modules. Relevant integral parameters are also determined. Before the time integration starts, the initial and boundary conditions of the aerodynamic scenario are defined. Algorithm 2 initializes the actual wind scenario on the basis of a read-in file (windDataIn.dat)

Algorithm 1: User-coding that initializes the rotor wall-adjacent body-force.

```

1 Module flow_solver():
  Input: nR // Number of rotors
  Input: nUpdate // Time step count for body force update
  Input: nSwapDir // Time step count for rotation direction check
  Input: nTurnOff // Time step count for turn-off check
2 PUBLIC iR // Rotor counter
3 PUBLIC nB, iB // Number of boundary faces and face counter
4 PUBLIC ci(nR,3), n(nR) // Rotational axis and speed per rotor
5 PUBLIC fi(nR,3) // Forces per rotor
6 PUBLIC Γtar(nR), Γis(nR), ratio(nR) // Target, actual and ratio of flow circulations
7
8 call init_flow_field() // initialize flow field, cf. Alg. 2
9 call init_body_force_field() // initialize body force field, cf. Alg. 3
10 for timeStep=1,nTimeSteps do
11   acquire new velocity  $v_i$  and pressure  $p$  values // Compute new flow field
12   call body_force_update() // Measure rotor forces and update the body force field, cf. Alg. 4

```

which, in addition to the ship's speed, primarily provides the wind speed and the angle of attack as well as data on the atmospheric profile. This process allows a high degree of automation of the investigations to be carried out. The apparent wind vector is defined and initialized with the help of a rotation matrix around the x_3 -axis.

Algorithm 2: User-coding that defines the flow field’s initial and boundary conditions.

```

1 Module init_flow_field():
   Input: windDataIn.dat // True wind data file
2 PRIVATE  $h^{\text{wind}}$  // Reference wind profile height [m]
3 PRIVATE  $v^{\text{wind}}(3)$  // Reference wind magnitude [m/s] at  $h^{\text{wind}}$ 
4 PRIVATE  $v^{\text{ship}}(3)$  // Ship speed [m/s]
5 PRIVATE  $\alpha^{\text{wind}}$  // True wind angle of attack [rad] measured from ship aft
6 PRIVATE mExp // Power-law exponent
7 PRIVATE  $D_{ik}(3,3)$  // Transformation matrix
8 PRIVATE  $p^{\text{ambient}}$  // Ambient pressure [Pa]
9
10  $v_1^{\text{ship}} \leftarrow \text{read}(\text{windDataIn.dat})$  // Read ship speed
11  $(v_1^{\text{wind}}, \alpha^{\text{wind}}, h^{\text{wind}}) \leftarrow \text{read}(\text{windDataIn.dat})$  // Read wind speed data
12  $p^{\text{ambient}} \leftarrow \text{read}(\text{windDataIn.dat})$  // Read ambient pressure
13
14  $D_{ik} = 0$ ;  $D_{11} = \cos(\alpha^{\text{wind}})$ ;  $D_{21} = \sin(\alpha^{\text{wind}})$  // Fill the rotation matrix
15  $D_{12} = -D_{21}$ ;  $D_{22} = D_{11}$ ;  $D_{33} = 1$  // Fill the rotation matrix
16  $v_1^{\text{wind}} = v_1^{\text{wind}}(x_3/h^{\text{wind}})^{\text{mExp}}$  // Atmospheric wind profile in  $x_1$  as function of  $x_3$  direction
17  $v_i = D_{ik}v_k^{\text{wind}} + v_i^{\text{ship}}$  // Define initial true wind field and boundary conditions
18
19  $p = p^{\text{ambient}}$  // Define initial pressure field and boundary conditions

```

The initial pressure field corresponds to the constant ambient pressure. Algorithm 3 first reads all relevant rotor and speed data from a second input file (rotorDataIn_rotorNumber.dat), whereby any number of rotors with different positions and speeds can be examined. The automatic determination of the horizontal rotor position using the zero and first geometric moment is worth mentioning. The same applies to the determination of the rotor axis. This simplifies the use of the overall process, as now only the rotor speed and a surface indicator are required to determine the surfaces associated with the rotor. Based on the data, the target circulation Γ^{target} of each rotor is calculated. Also, the momentum source in the first computational cells above the rotor wall is initialized appropriately in circumferential direction. In the last algorithm, the actual control of the Flettner rotors is carried out. For this purpose, the current circulations Γ^{actual} are calculated every time step. The deviation from the target circulations defined in Alg. 2 is considered every #nUpdate time step, and the ratio scales the volume force appropriately. In the ideal, converged state, the ratio reads one. However, actual investigations, especially at high spinning ratios, show a slight fluctuation around the unit value. Since the averaging of rotor forces is also carried out in Alg. 3, two further features have been implemented. If the propulsive force is negative up to a specific number of time steps (#nSwapDir), the current rotational direction seems to not generate thrust but resistance, so that a single change of the ratio variable reverses the direction of rotation. If the rotor still generates resistance (#nTurnOff), the rotor is deactivated by setting the ratio variable to zero. Both features can be deactivated by selecting the appropriate variables. Typical values of #nSwapDir and #nTurnOff are chosen, such that 5-10 equivalent rotor flows are considered.

3 Concept Validation and Calibration

3.1 2D Flow Around Rotating Circular Cylinder

First, we start with an academic case considering the flow-potential-based investigation of a rotating (n) circular cylinder of diameter D in a free stream with homogeneous velocity V . For the case sketched on the left in Fig. 1, analytical solutions for the velocity and pressure field can be derived, providing information about the resulting drag (f_d) and lift (f_l) forces, especially as a function of the rotor’s rotational speed. An exemplary, unstructured numerical grid is shown on the right. The grid consists of approximately 9500 finite volumes and is refined towards the cylinder, whereby the cylinder circumference is discretized with roughly 750 cells.

The section’s main focus is on the behavior of the rotating cylinder’s lift and drag coefficients as a function

Algorithm 3: Pseudo-code to initialize the rotor-wall adjacent body-force based on the rotor's rotational rate.

```

1 Module init_body_force_field():
  Input: rotorDataIn_*nR*.dat // number of Rotors and input files
2  PRIVATE  $l, m_i(3)$  // Geometrical moments
3
4   $f_i(\cdot) = 0, \Gamma^{\text{tar}}(\cdot) = 0, \text{ratio}(\cdot) = 0$  // Initialize rotor forces, target circulations, and ratios
5  for  $iR=1, nR$  do
6     $n(iR) \leftarrow \text{read}(\text{rotorDataIn}_*iR*.dat)$  // Read rotor rotation rate
7     $l = 0, m_i = 0$  // Initialize geometrical moments
8    for  $iB=1, nB$  do
9      if  $iB$  belongs to  $iR$  then
10        $l = l + \sqrt{\Delta\Gamma_i^{iB} \Delta\Gamma_i^{iB}}$  // Update zeroth geometrical moment
11        $m_i = m_i + \sqrt{\Delta\Gamma_i^{iB} \Delta\Gamma_i^{iB}} x_i^{iB}$  // Update first geometrical moment
12      $o_i = m_i/l$  // Compute geometric center
13      $\omega_i = 0; \omega_3 = 2\pi n(iR)$  // Compute rotation vector
14      $c_i(iR) = \omega_i/|\omega_i|$  // Compute rotational axis
15     for  $iB=1, nB$  do
16       if  $iB$  belongs to  $iR$  then
17          $v_i^{iB} = \omega_i \times (x_i^{iB} - o_i)$  // Circumferential rotor velocity
18          $\Gamma^{\text{tar}}(iR) = \Gamma^{\text{tar}}(iR) + v_i^{iB}(\Delta\Gamma_k^{iB} \times c_k(iR))_i$  // Update target circulation
19          $b_i^{iB} = \rho v_i^{iB}$  // Initial guess for momentum source (check dimensions)

```

Algorithm 4: Pseudo-code to update the rotor-wall adjacent body-force.

```

1 Module body_force_update():
2   $\Gamma^{\text{is}} = 0$  // Initialize actual circulations
3  for  $iR=1, nR$  do
4    for  $iB=1, nB$  do
5      if  $iB$  belongs to  $iR$  then
6         $\Gamma^{\text{is}}(iR) = \Gamma^{\text{is}}(iR) + v_i^{iB}(\Delta\Gamma_k^{iB} \times c_k(iR))_i$  // update target circulation
7         $f_i(iR) = f_i(iR) + p(iB) \Delta\Gamma_i(iB)$  // Update rotor forces
8     $\text{ratio}(iR) = |\Gamma^{\text{tar}}(iR)/\Gamma^{\text{is}}(iR)|$ 
9    if  $\text{mod}(\text{timestep}, n\text{Update}) = 0$  then
10      $f_i(iR) = f_i(iR)/n\text{Update}$  // Compute mean rotor forces
11     IF (  $\text{timestep} = n\text{SwapDir}$  & (  $f_1(iR) < -10^{-3}$  ) )  $\text{ratio}(iR) = -\text{ratio}(iR)$  // Swap rotation
12     IF (  $\text{timestep} = n\text{TurnOff}$  & (  $f_1(iR) < -10^{-3}$  ) )  $\text{ratio}(iR) = 0$  // Turn rotor off
13     for  $iB=1, nB$  do
14       if  $iB$  belongs to  $iR$  then
15          $b_i(iB) = b_i(iB) \text{ratio}(iR)$  // Update body force magnitude
16      $f_i(iR) = 0$  // Re-initialize rotor forces

```

of the spinning ratio, which are defined for the paper's remainder as follows:

$$c_d = \frac{2f_d}{\rho V^2 DH}, \quad c_l = \frac{2f_l}{\rho V^2 DH} \quad \text{and} \quad k = \frac{\pi n D}{V}. \quad (12)$$

This section's benchmark values refer to the ideal, potential-flow-based relation, i.e., $c_l(k) = 2\pi k$ and $c_d(k) = 0$.

Figure 2 shows an exemplary response of the proposed dynamic rotor rotation adjustment procedure outlined in Chapter 2.3 (cf. Algs. 1 - 4) with UD approximation, i.e., $\beta = 1$ in Eqn. (9). For three spin ratios, the development of the ratio of the target/actual flow circulation (cf. Eqn. (7)), the lift coefficient, and the drag coefficient are depicted over the simulated time steps from left to right, respectively. The discrete markings

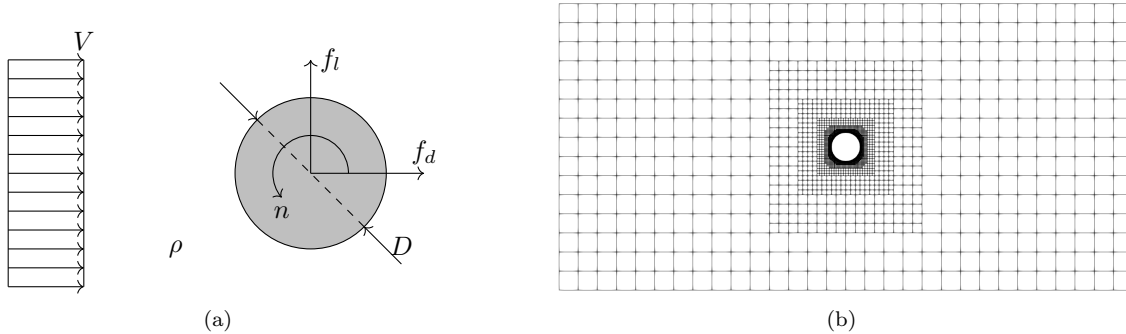


Figure 1: Two dimensional circular cylinder case: Schematic representation of (a) the overall setup and (b) of the utilized numerical grid.

indicate the adjustment of the volume force every 100-time steps, cf. Alg. 4. All three circulation ratios start at circulations that are more than one magnitude too small and converge to the targeted unit ratio within the first 1000 time steps. This convergence can also be observed in the lift and drag coefficients, which reach a plateau with a slight delay. As expected, the lift coefficient increases for higher spin ratios, whereby the lift coefficients are more than an order of magnitude higher than their drag companions. The latter are different from zero, indicating the violation of the inviscid flow assumption. This is due, in particular, to the upwind-biased approximation of the convective term used and the associated introduction of a solid numerical diffusion.

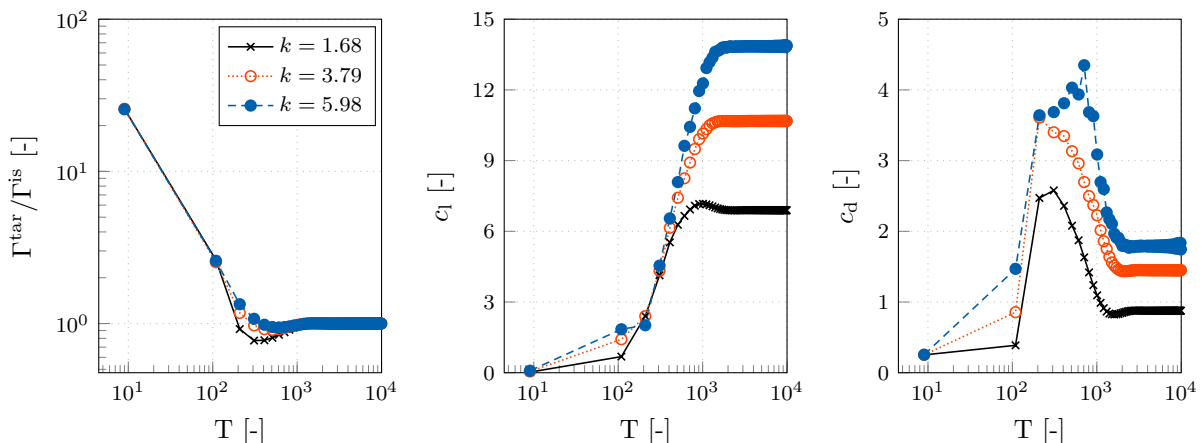


Figure 2: Two dimensional circular cylinder case: Exemplary development of (left) the ratio of the target/actual flow circulation, (center) the lift coefficient, and (right) the drag coefficient over the simulated time steps.

The exemplary investigation is consistently continued for different spinning ratios in the interval $0 \leq k \leq 8$, whereby different aspects of the numerical process, like the resolution of the outer iterative method or different convection schemes, are considered. Temporal and spatial discretization influences have been eliminated in a preceding grid and time step study. The time step is chosen to discretize one equivalent flow based on the free stream velocity with approximately 100-time steps. The numerical responses tend to fluctuate, especially for higher spinning ratios, so results are averaged over the last 5 equivalent flows, i.e., 500-time steps.

First, the flux blending approach from Eqn. (9) is examined for seven UD/CD ratios based on the blending parameter β such that 100 (0) up to 5 (95) percent upwind (central) differencing are examined. The limit case of 0 (100) percent UD (CD) tends to produce numerical instabilities and is thus not considered. Resulting lift and drag coefficients are shown in Fig. 3 on the left and right over the spinning ratio, respectively. Additionally, the reference potential flow results are included. An increase in the CD/UD ratio leads to a moderate increase in the lift and a reduction in the drag coefficient. While the differences in the lift coefficient become visible from a spinning ratio of $k \geq 1$, the differences in the drag companion are visible across the entire spinning ratio spectrum and are much more pronounced. The results align with theoretical considerations, which dictate a

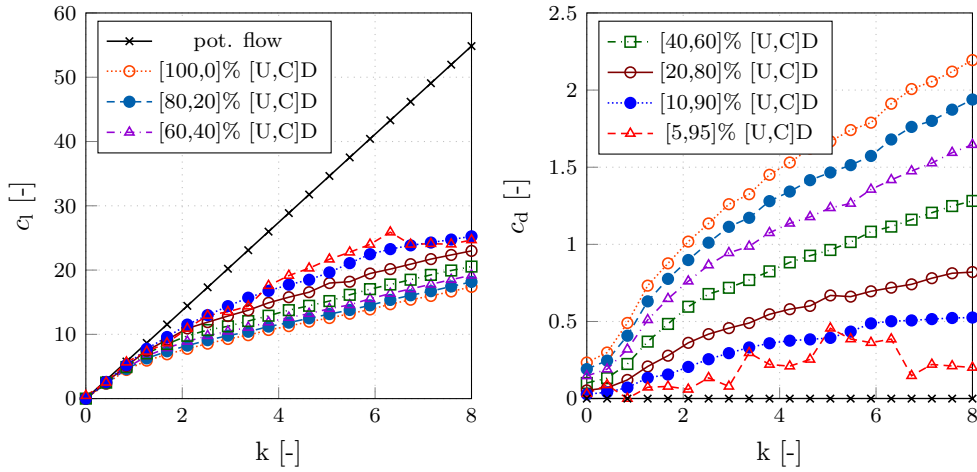


Figure 3: Two dimensional circular cylinder case: Predicted lift (left) and drag (right) coefficient over the spinning ratio for different Upwind Differencing (UD) and Central Differencing (CD) ratios to approximate the convective momentum transport.

decreased numerical viscosity for reduced upwind proportions.

In the following, in addition to the 10/90 % UD/CD ($\beta = 0.1$) flux blending case, TVD scenarios with $\kappa = 0.5$ and $\kappa = 1.0$ are examined, whereby the number of fixed, enforced outer iterations is varied, i.e., $M = [2, 4, 6, 8]$. The investigations are intended to check whether the numerical effort can be reduced by decreasing the convergence per time step while maintaining the quality of the results. The results are shown in Fig. 4 for the lift coefficient and in Fig. 5 for the drag coefficient, with the flux-blending results on the left, the TVD-QUICK results in the middle, and the TVD-CD results on the right. Minor differences can be identified in the lift coefficient between the investigations at different numbers of outer iterations, which are particularly pronounced at higher spinning ratios. Up to $k = 4$, hardly any differences are recognizable in both coefficients. Instead, predictions from the employed convection schemes differ: While the lift coefficients of the flux-blending investigations correspond to the results from Fig. 3 and visibly deviate from the flow-potential-based reference results for $k \geq 2$, the TVD investigations align with the reference results for higher spinning ratios. Predictions of the TVD-CD method also deviate from the benchmark results for $k \geq 2$ but still follow the reference trend with a less reduced slope. The TVD-QUICK method's results align mostly perfectly with the reference lift results up to $k \leq 4$ and are still close to $k \leq 6$. The differences between both TVD approaches indicate that the TVD-CD method increasingly switches dynamically to low-order, UD-biased approximations. Results of the predicted resistance coefficients in Fig. 5 allow similar conclusions. Note: Due to considerably

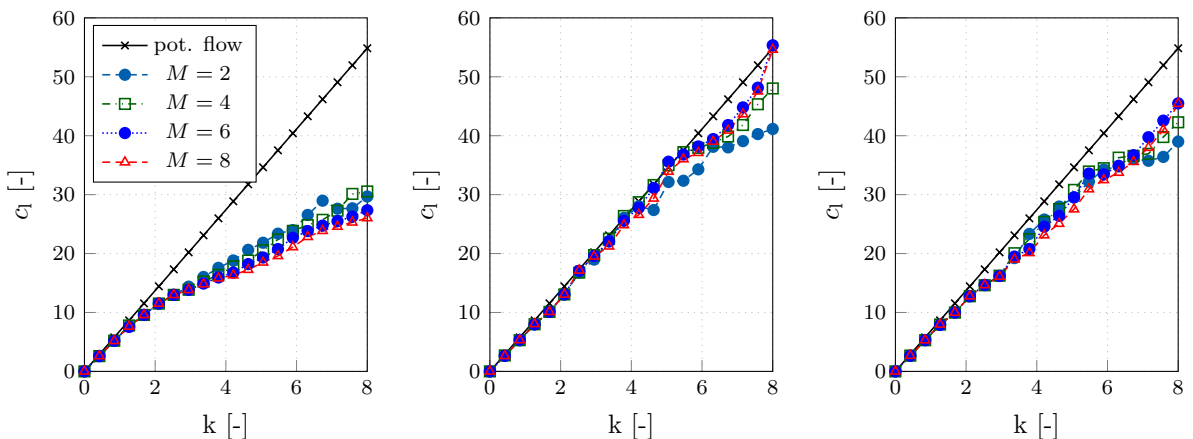


Figure 4: Two dimensional circular cylinder case: Lift coefficient for different fixed outer iterations over the spinning ratio for (left) a flux blending case with 10/90 percent UD/CD ($\beta = 0.1$), (center) a TVD-QUICK approach with $\kappa = 0.5$, and (right) a TVD-CD case with $\kappa = 1.0$.

less numerical diffusion, the y-axis represents a smaller interval than in Fig. 3 (right). The TVD methods generally outperform the flux-blending approach up to $k \leq 4$ with hardly any difference between the results for different numbers of outer iterations. For increased spinning ratios $k \geq 4$, the different studies provide stronger deviating predictions, which are additionally subject to solid fluctuations, that are highest for several (a few) outer iterations in the case of the TVD-based (flux-blending) investigations. Additionally, the increase in the drag coefficient for TVD-CD starts somewhat earlier at $k = 1$ than at $k = 2$ for TVD-QUICK. However, TVD-CD results feature a smaller slope, resulting in a slightly lower drag coefficients for $k = 4$.

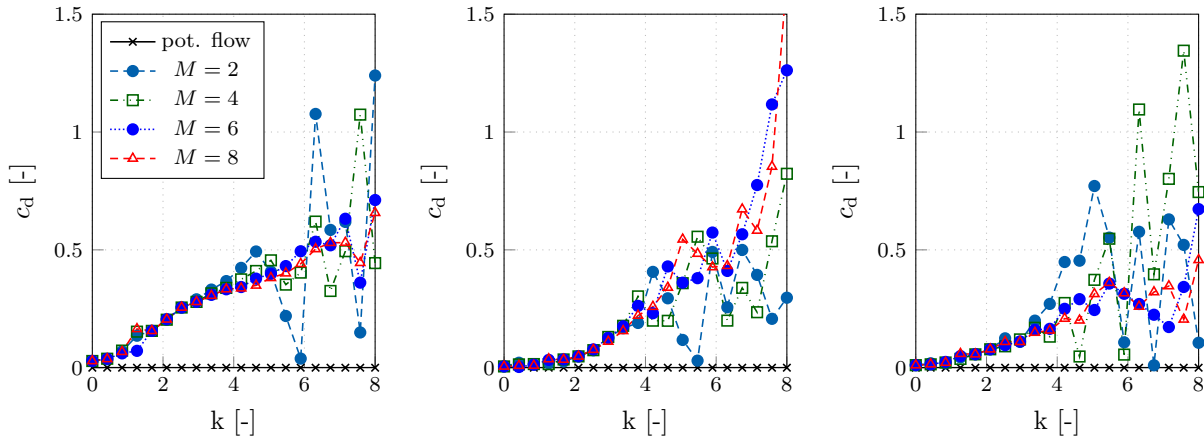


Figure 5: Two dimensional circular cylinder case: Drag coefficient for different fixed outer iterations over the spinning ratio for (left) a flux blending case with 10/90 percent UD/CD ($\beta = 0.1$), (center) a TVD-QUICK approach with $\kappa = 0.5$, and (right) a TVD-CD case with $\kappa = 1.0$.

A summary in between: About 10-20 adjustments of the near-cylinder volume force seem necessary to adjust the actual circulation to the target value. Furthermore, the numerical effort can be significantly reduced by not converging reasonably every time step. However, fixed 2-4 outer iterations are sufficient for solid predictions, especially in the technically relevant spinning ratio range up to $k \leq 4$. The closest solutions to the ideal flow-potential-based reference data are predicted by the TVD-QUICK method, where the lift results are remarkably well reproduced up to $k = 5$ for the lift coefficient and up to $k = 2$ for the drag companion. In contrast, all investigated flux-blending procedures introduce a solid amount of numerical viscosity into the numerical system, resulting in significantly increased drag coefficients and, at the same time, reduced lift coefficients, already at moderate ($k = 2$) and especially at increased ($k = 4$) spinning ratios. However, compared to the idealized, inviscid flow assumption, this deficiency can be exploited by suitable model calibration for real-world, viscous applications.

3.2 Single 3D Flow Rotor in Idealized Conditions with Two End-Plates

This section increases the complexity by conducting a three-dimensional investigation on a full-scale Flettner rotor in idealized wind tunnel conditions. The effort's primary aim refers to the prediction quality of three-dimensional flow effects.

The considered rotor features an aspect ratio of $H/D = 6$ and is equipped with two identical upper and lower end plates, whereby the end plate to rotor diameter ratio is $D_{\text{endplate}}/D_{\text{rotor}} = 2$. The lower end plate is placed at $H/9$, and both end plates have a height of $H_{\text{endplate}}/H_{\text{rotor}} = 0.005$. The far-field boundaries are placed one hundred rotor diameters away from the rotor to minimize the blockage effect. The incoming wind features an atmospheric profile with $h^{\text{wind}}/H_{\text{rotor}} = 1/2$ and $\text{mExp} = 0.085$, cf. Alg. 2. An exemplary impression of a utilized numerical grid of medium resolution with approx. 30 000 control volumes is provided in Fig. 6 for (a) the near field and (b) the far field. The wind profile is sampled with 20 control volumes.

High-fidelity results from a hybrid averaged/filtered RANS/LES analysis at $\text{Re}_D = 2 \cdot 10^6$ or $\text{Re}_H = 1.2 \cdot 10^7$ serve as benchmark data. An impression of the corresponding numerical grid is shown in Fig. 7 (a), where the near rotor and the wake region are considerably more refined compared to the Eulerian grid, cf. Fig. 6 (a). The grid consists of approx. 11 million control volumes. The figure on the right provides an instantaneous impression of the scale-resolving simulation at $k = 3$ based on $Q = 100$ iso-lines of the Q -vortex-criterion, where

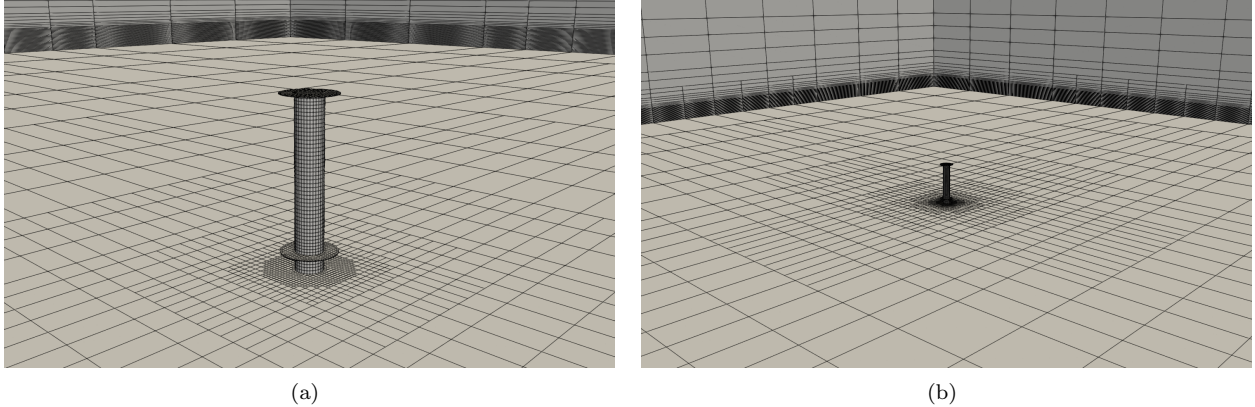


Figure 6: Single rotor flow: Perspective view of a medium-sized numerical (a) near and (b) far-field grid.

the local vorticity colors the iso-lines. In addition to the smaller vortices in the rotor wake, the tip vortex at the rotor end is particularly recognizable.

In the following, the spinning ratio spectrum of $0 \leq k \leq 6$ is considered in $\Delta k = 0.5$ steps, whereby three different strategies for approximating the convective momentum transport are investigated. In addition to the pure UDS method ($\beta = 1$), the κ -scheme for QUICK ($\kappa = 0.5$) and CDS ($\kappa = 1.0$) is assessed. Three numerical grids with different resolutions are considered: While grid 1 discretizes the rotor with about 25 discrete elements and the entire field with about 20 000 control volumes, grid 2 increases this to 50 as well as 40 000 and grid three to 100 as well as 80 000 cells, respectively. Hence, a total of $13 \times 3 \times 3 = 107$ Eulerian and 13 scale-resolving simulations are carried out. The Eulerian simulations adjust the rotor circulation every 100 time steps. The time step is set for the Eulerian and the scale-resolving simulations so that 100-time steps sample a fluid particle's equivalent rotor passing. Both methods simulate 200 equivalent rotor flows, whereby the Eulerian simulations seek for pseudo steady results and thus consistently perform only three outer iterations per time step, cf. results from Sec. 3.1, e.g., Fig. 4. The scale-resolving simulations have an increased convergence rigor and require a relative residual decrease per equation of at least two orders of magnitude per time step, which, for the chosen relaxation parametric, leads to an increased numerical effort of approx. 10 outer iterations per time step. Local and integral flow data are averaged over the last 20 equivalent rotor flows.

Figure 8 presents the predicted drag coefficients over the spinning ratio for all scrutinized grids, distinguishing between the UDS method (left, $\beta = 1$), the QUICK (center, $\kappa = 0.5$), and the CDS method (right, $\kappa = 1.0$) for approximating the convective momentum transport. Results of the smallest (middle) [coarsest] grid are shown in blue solid with filled circles (orange dotted with circles) [green dashed with squares], and all ordinates are equally scaled. The viscous reference results are shown in black solid lines with crossed marks. Generally, an increase in the drag coefficient can be observed in all cases for rising spinning ratios. However, all Eulerian results significantly overshoot the viscous reference results. The drag coefficient for the finest considered grid (level three) tends to be the smallest, especially for high spinning ratios. Additionally, the drag results of the UDS studies appear to be lower than those of the two κ -scheme-based studies.

The predictions of the associated lift coefficients are shown analogously in Fig. 9. In line with the drag results, the Eulerian investigations' lift predictions are likewise significantly overestimated compared to the

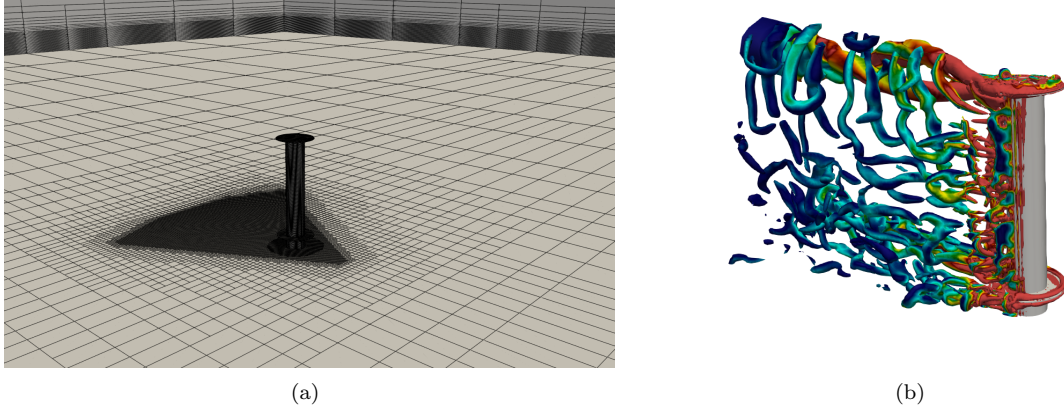


Figure 7: Single rotor flow: Perspective view of the near-field grid and (b) instantaneous vortex structures colored with the vorticity magnitude of a hybrid averaged/filtered RANS/LES reference simulation at $Re_H = 1.2 \cdot 10^7$ or $Re_D = 2 \cdot 10^6$ at $k = 3.0$.

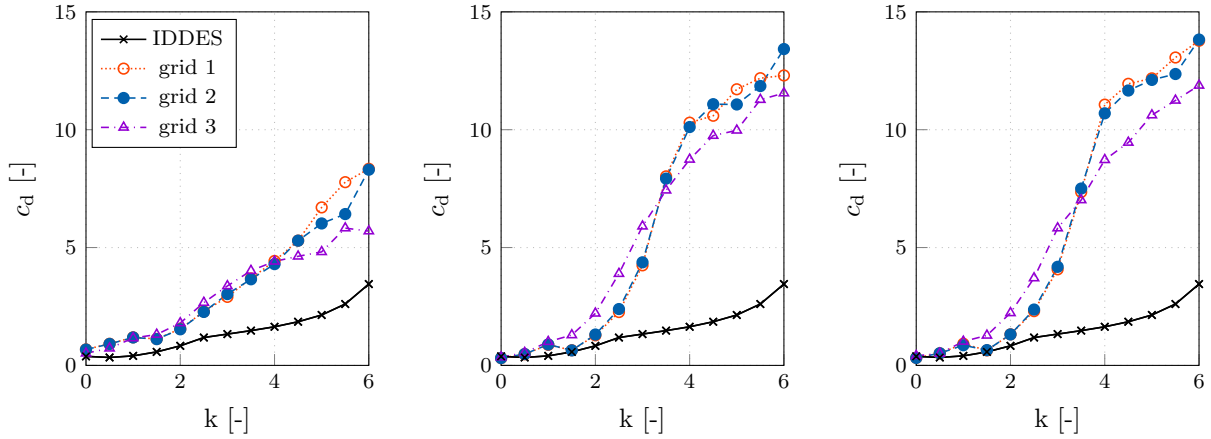


Figure 8: Single rotor flow: Drag coefficient over the spinning ratio predicted by Eulerian tests on four different grids for a UDS (left), QUICK (center), and CDS (right) approach. In addition, the same viscous reference result is shown.

viscous reference results, especially for high spinning ratios. Predictions based on the UDS method increase almost linearly for increasing spinning ratios and are close to the viscous reference results up to approximately $k = 2$. Furthermore, in the UDS case, the finest grid provides larger [smaller] lift coefficients for smaller [larger] spinning ratios. The two further investigations based on the κ -scheme show an almost linear increase with, compared to UDS, an increased slope up to approx. $k = 3.5$, which abruptly ends and starts forming a plateau. For large spinning ratios around $k = 6$, inviscid predicted lift coefficients approach the viscous reference results.

In addition, the predictions of the κ -scheme-based investigations in the plateau region for $4 \leq k \leq 6$ are of the same order of magnitude as the UDS-based predictions, which indicates an increased switching from QUICK/CDS to UDS, i.e., from high-order to low-order convection. For the high-order convection studies, the lift predictions appear less sensitive to spatial discretization than their drag predictions.

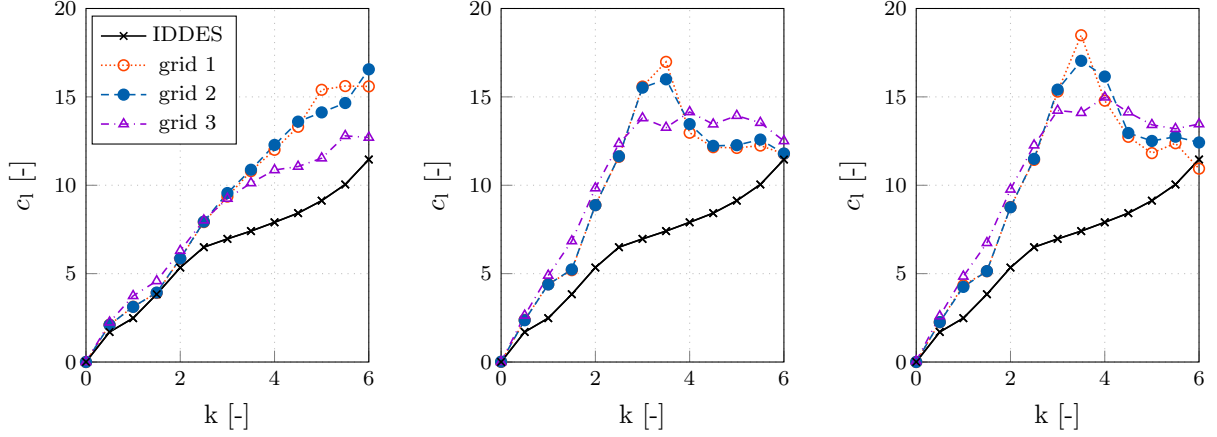


Figure 9: Single rotor flow: Lift coefficient over the spinning ratio predicted by Eulerian tests on four different grids for a UDS (left), QUICK (center), and CDS (right) approach. In addition, the same viscous reference result is shown.

The Eulerian investigations' inflated lift and drag predictions will be discussed below. The increase in lift is due to the idealized flow assumption in combination with the utilized frictionless simulation method. Strictly speaking, the Eulerian method cannot provide parasitic resistances, which occur in isolation for a fixed rotor at $k = 0$. Figure 10 shows the relative deviations $(c_d^{\text{EUL.}} - c_d^{\text{IDDES}}) / c_d^{\text{IDDES}} \cdot 100$ [%] of each inviscid investigation from the reference IDDES investigations. As can already be seen from the raw data in Figs. 8-9, the error values are in the high three-digit range, reaching 200 percent for the UDS-based investigations and even up to 500 percent for the high-order convection investigations. Particular attention should be paid to situations with a stationary rotor at $k = 0$: The relative errors of the high-order methods change their sign, i.e., the inviscid QUICK and CDS analyses underestimate the IDDES-based drag coefficient. This aligns with theoretical considerations for inviscid analysis. Still, a parasitic resistance-free simulation can hardly be constructed with the utilized FVM. The increased numerical viscosity of the UDS-based investigations already provides a slightly increased drag coefficient for a non-rotating rotor. Figure 11 gives an analogous illustration of the relative error of the lift

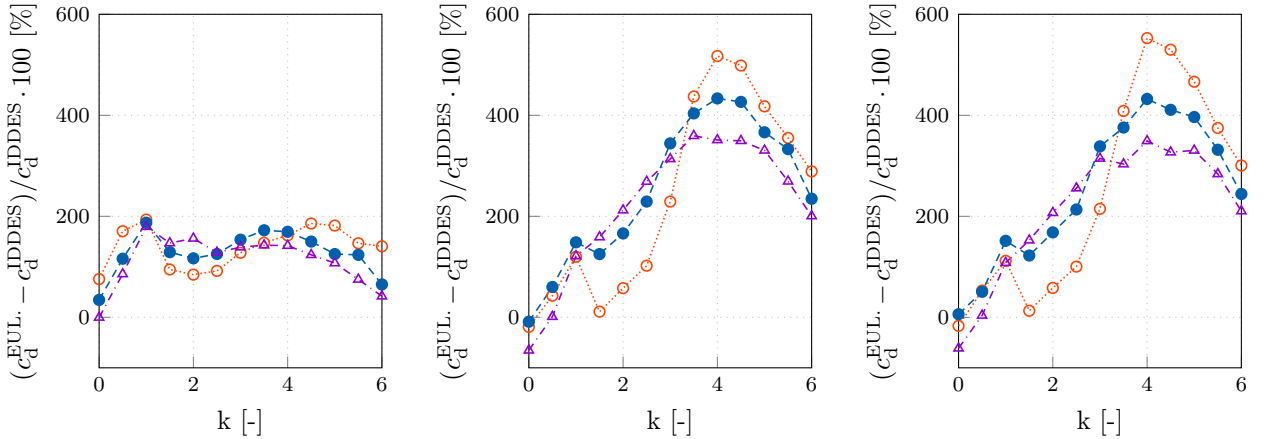


Figure 10: Single rotor flow: Relative error in the drag coefficient between the viscous reference simulation and the Eulerian approach on three different grids for a UDS (left), QUICK (center), and CDS (right) approach over the spinning ratio.

coefficient predictions. Again, errors for the UDS-based studies are more minor than those of the high-order convection studies, with all three studies generating reduced relative errors for large spinning ratios. In the moderate spinning ratio range, errors of the κ -scheme-based methods are approximately twice as large as those of the UDS-based study.

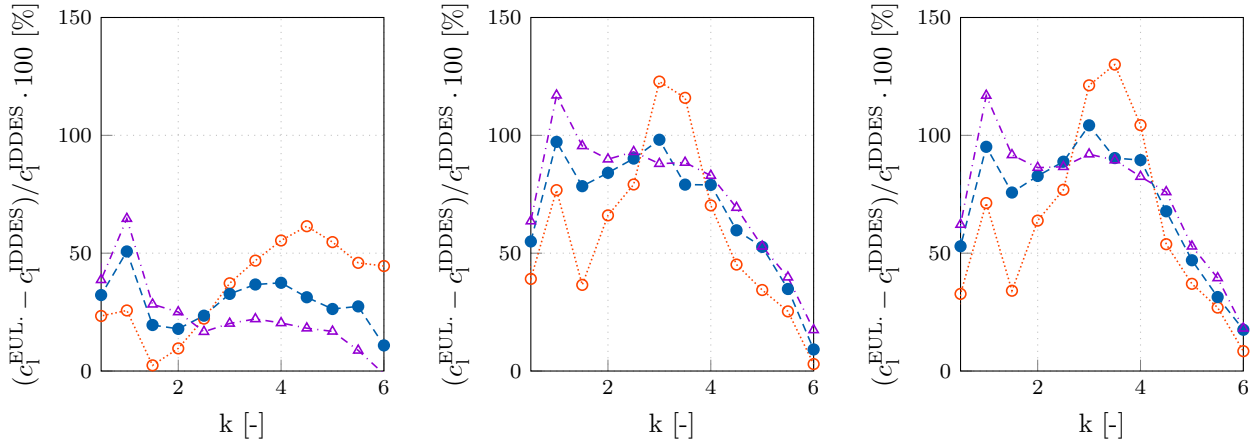


Figure 11: Single rotor flow: Relative error in the lift coefficient between the viscous reference simulation and the Eulerian approach on three different grids for a UDS (left), QUICK (center), and CDS (right) approach over the spinning ratio.

The fundamentally low parasitic drag for $k = 0$, coupled with the significantly increased drag coefficients for $k > 0$ as well as the increased lift coefficient, indicates a dominant influence of induced drag components. Based on considerations from lifting-line theory, this subsection's remainder will examine the quadratic relationship between the lift and induced drag coefficients, i.e., $c_{d,i} = \propto c_l^2$. For this purpose, all Eulerian simulations are repeated, but the approximation of the momentum in the rotor axis direction (x_3 direction) is suppressed, resembling a pseudo 2D or 2.5 D investigation, that should suppress the generation of 3D tip vortices and drive the simulation results closer to flow potential-based results. Analogous to Figs. 8-9, Figs. 12 and 13 provide the drag and lift coefficients over the considered spinning ratios for the pseudo 2D studies, distinguishing from left to right between UDS, QUICK, and CDS-based investigations. While the drag coefficients are significantly reduced towards the order of magnitude of the viscous reference studies, the lift coefficients are particularly increased and rise almost constantly when increasing the spinning ratio, especially for the κ -scheme-based investigations. In comparison, the UDS-based methods yield reduced lift but increased drag coefficients. Overall, the pseudo-2D results are similar to the results of the circular cylinder study from the previous Sec. 3.1.

Two results of two induced-drag coefficient $c_{d,i}$ estimation approaches are presented in Fig. 14 (left) over the spinning ratio, which (a, with marks) form the difference of the drag coefficients from the 3D (cf. Fig. 8) to the 2D (cf. Fig. 12) investigations, i.e., $c_{d,3D} - c_{d,2D}$ and (b, without marks) assume a scaled, squared correlation with the lift coefficient. The latter argumentation assumes a vanishing parasitic resistance at, i.e., $c_{d,2D}(k = 0) = 0$ in line with lifting line arguments. All three investigated convection schemes are considered on the finest numerical grid. Both induced drag measures predict almost identical values up to a spinning ratio of $k = 3$ and only start deviating for higher spinning ratios, with the bifurcation in the UDS investigations even being shifted to approx. $k = 4$. For high spinning ratios, all induced drag estimates based on the lifting line theory tend towards a value of $c_{d,i} \approx 5$. The 3D-2D difference results of the κ -scheme investigations overshoot this and reach twice as high values around $c_{d,i} \approx 10$. In contrast, the values of the UDS investigations drop to $c_{d,i} \approx 2$. Finally, the estimated induced drag coefficients are related to their parasitic companion to estimate a realized rotor efficiency in Fig. 14 (right). The metric is similar to the Oswald factor of classic lifting line assumptions. The parasitic reference resistance is taken from the IDDES investigation on the non-rotating rotor cf. black reference values in Figs. 8 and 12 at $k = 0$, multiplied by the rotor's aspect ratio times pi. Both rotor efficiencies of the κ -scheme-based investigations are again similar and of the same order of magnitude. They reach an almost constant value of $c_l^2 / (H/D\pi c_{d,IDDES,k=0}) = \mathcal{O}(27)$ for $k \geq 3$. In contrast, the efficiency of the UDS-based investigations is significantly reduced, and $c_l^2 / (H/D\pi c_{d,IDDES,k=0}) = \mathcal{O}(27)$ is reached for the highest spinning ratios $k \geq 5.5$ considered only. Compared to classic profile flows, the comparatively high rotor efficiency can be attributed to (a) the additional momentum input of the mechanically spinning rotor and (b)

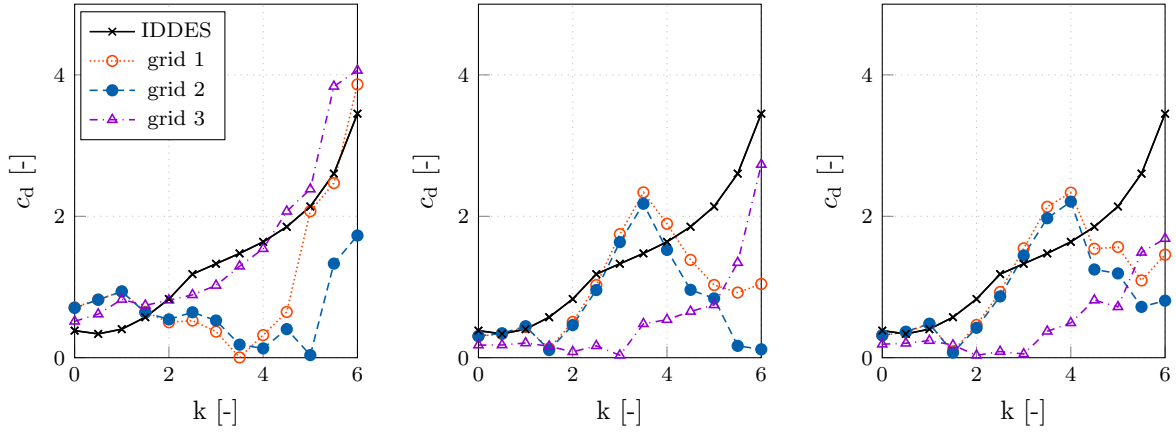


Figure 12: Single rotor flow (pseudo 2D): Drag coefficient over the spinning ratio predicted by Eulerian tests on four different grids for a UDS (left), QUICK (center), and CDS (right) approach, skipping the momentum balance in the rotor axis direction. In addition, the same viscous reference result is shown.

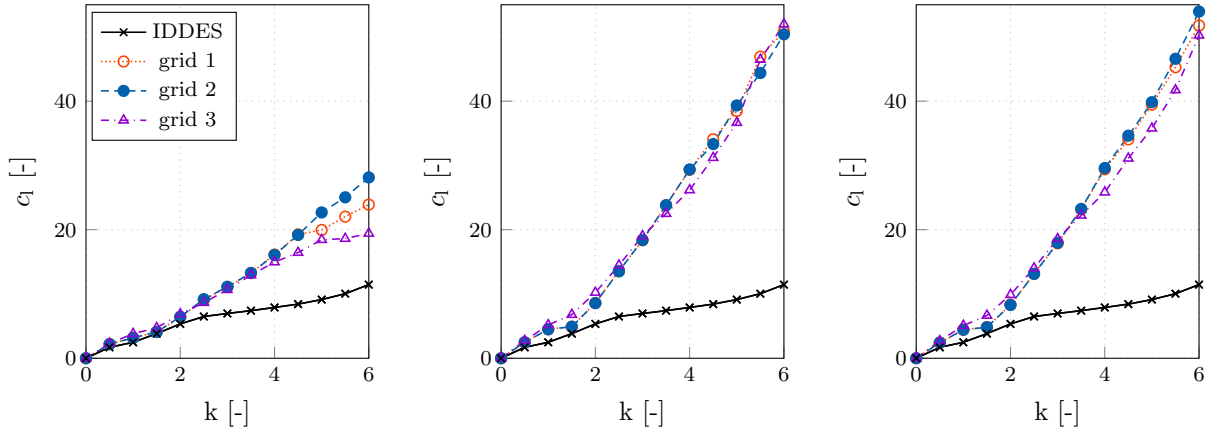


Figure 13: Single rotor flow (pseudo 2D): Lift coefficient over the spinning ratio predicted by Eulerian tests on four different grids for a UDS (left), QUICK (center), and CDS (right) approach, skipping the momentum balance in the rotor axis direction. In addition, the same viscous reference result is shown.

the neglect of viscous effects.

A short conclusion in between is: Since the high-order-convective methods based on the κ -scheme introduce significantly less numerical viscosity into the discrete system, these scenarios provide significantly increased lift coefficients, which are close to the flow-potential-based reference results for academic 2D investigations on a circular cylinder. However, in a three-dimensional context, the presented method can adequately reproduce induced resistances, especially the quadratic relation between induced drag and lift, i.e., $c_d \propto c_l^2$, which in turn leads to a solid overestimation of drag coefficients, especially for high spinning ratios. The lift and drag overestimation is reduced for low-order-convective-based approaches, introducing increased numerical viscosity. Influences of the spatial discretization cannot be excluded entirely. However, the influence of the convection scheme seems significantly increased, especially since the primary purpose refers to a rough relative rotor performance prediction.

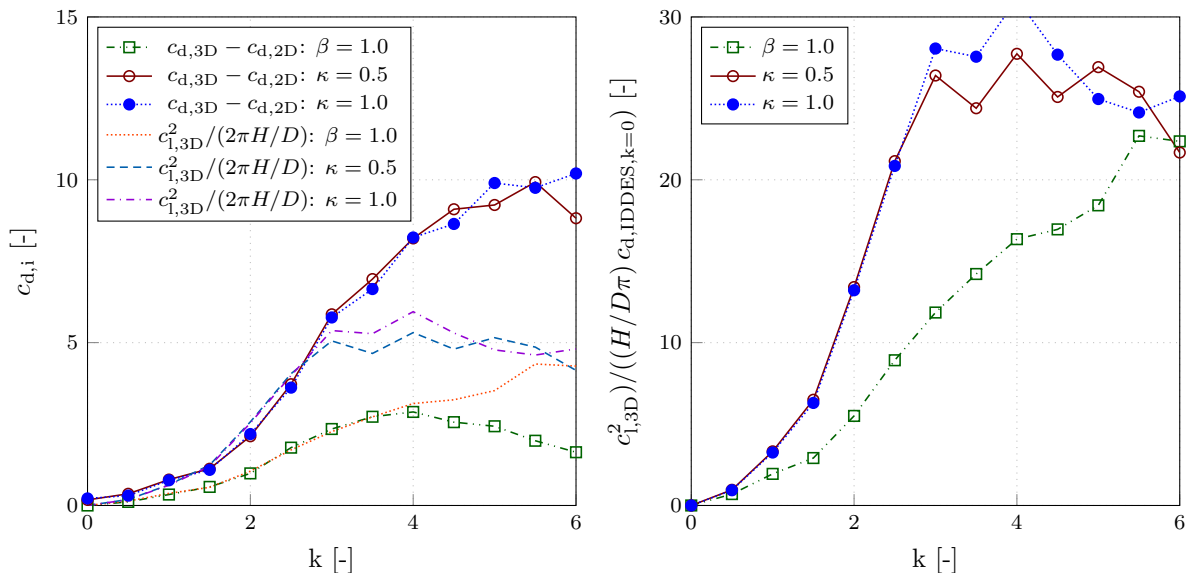


Figure 14: Single rotor flow: Estimated (left) induced drag for two measures and (right) rotor efficiency based on a parasitic component from an IDDES simulation at rotor rest over the spinning ratio for three discrete approximation strategies on the finest grid.

4 3D Flow Around a General Cargo Ship at Realistic Operation Conditions

Finally, the complexity of the validation is further increased by examining a real operating vessel equipped with Flettner rotors. For the paper's analysis, accurate ship data is used to investigate suitable operating conditions: The vessel is traveling at 6.8 knots with a draft of 6m without trim in a wind of 8 m/s (Beaufort 5). The wind profile is approximated using an atmospheric profile with $h^{\text{wind}} = 20$ m as well as $m\text{Exp} = 0.085$ (cf. Alg. 2), and the True/Apparent Wind Angle (T/AWA) of attack varies in the study. The Flettner rotor of Diameter D has a constant speed of $n = 176$ rpm. Based on the operating data, the ship cruises at $\text{Re}_{L_{pp}} = V_{\text{wind}} L_{pp} / \nu_{\text{air}} \approx 1.039 \times 10^8$ and the rotor operates at $k = \pi n D / V_{\text{wind}} \approx 2.4$, where ν_{air} , L_{pp} , and V refer to the dynamic viscosity of air, the ship's length between the perpendiculars and a representative apparent wind magnitude 10m over ground, respectively.

The investigations are carried out on three unstructured numerical grids of varying fineness along and near the rotor. The ship is discretized in the longitudinal direction with approx. 225 cells, whereby finer geometric details are treated more precisely. In general, the grid is coarsened away from the ship. The three different grids vary only in their resolution of the Flettner rotor, which is discretized with either 25, 50, or 100 cells in the circumferential and normal directions so that the three grids consist of approx. 585 000, 695 000, and 995 000 cells. An impression of the surface ship is provided in Fig. 15 for (a) the front, (b) the starboard side, and (c) the top view, where the surface discretization of the second grid refinement is depicted. The corresponding discretization of the outer far-field is shown in Fig. 16, which also indicates the refinement in the atmospheric wind profile region. The investigated domain extends over a length, width, and height of 11, 11, and 5 ship lengths, respectively, with the ship placed centered at the lower end. The aerodynamic investigations are based on an undeflected free water surface, which is treated as a symmetry boundary condition at the lower end of the domain. A constant pressure is specified at the upper end, and the apparent wind (i.e., superposition of ship and wind speed) is specified as a superposition along all horizontal outer boundaries, cf. Alg. 2. Initial conditions follow the far field apparent wind boundary conditions. The time step is chosen such that an equivalent flow around the ship is sampled with approximately 150-time steps. Each inviscid simulation is performed for $T = 3000$ time steps. Results are averaged over the last 10 equivalent flows, i.e., 1500 time steps.

To assess the quality of the method proposed in this paper, reference results on the general cargo vessel follow hybrid averaged/filtered RANS/LES simulations in line with the Improved Delayed Detached Eddy Simulation (IDDES) approach, cf. Gritskevich et al. (2012) or Pache and Rung (2022); Kühl (2025). Their spatial and temporal discretization differs significantly from the inviscid investigations. A perspective impression of the utilized surface grid is given in Fig. 17 (left) and indicates an intensified refinement in regions close to the ship.

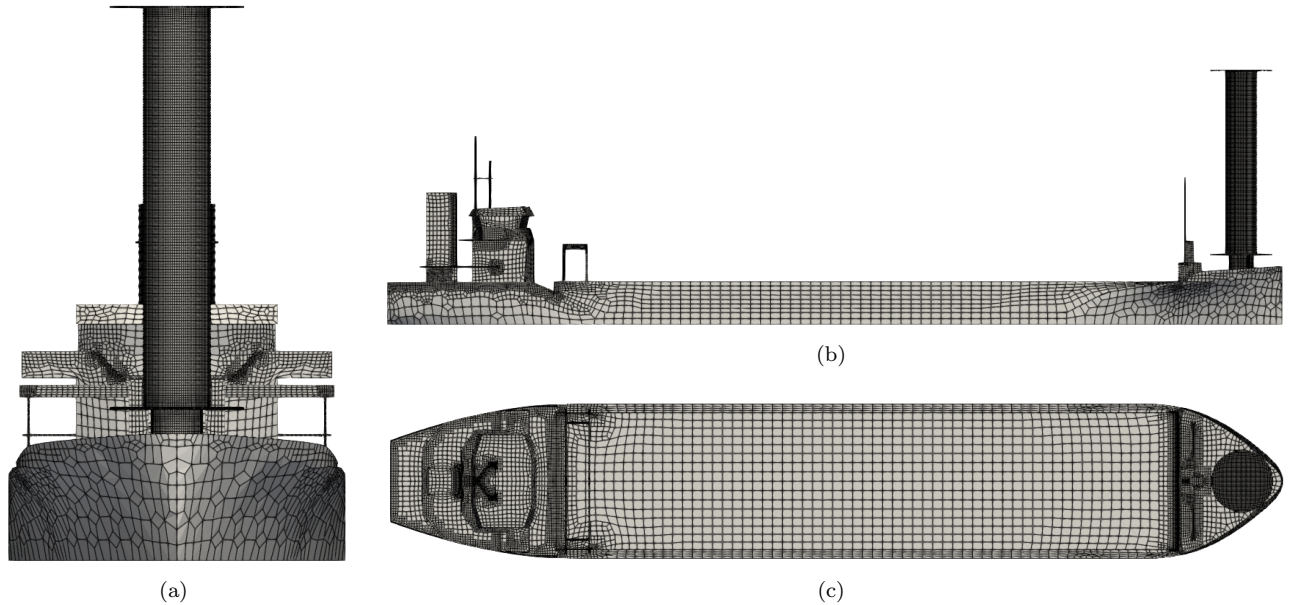


Figure 15: General cargo ship flow: The utilized surface discretization presented from (a) front, (b) starboard side, and (c) top.

The refinement sphere around the ship's midpoint is discretized with $\Delta x_1/L_{pp} = \Delta x_2/L_{pp} = \Delta x_3/L_{pp} = 225$. In combination with the additional required refinement in the wall-normal direction, which allows the use of wall functions by suitable values of $y^+ \approx 50$, this results in an increased numerical grid with approximately eleven million control volumes. The time step is reduced to comply with an averaged Courant number below one, resulting in an increased number of $T = 90\,000$ time steps. In each time step, all residuals are reduced by at least two orders of magnitude. Further details, such as an increase of the temporal approximation order by a third time level or the use of 20/80 percent QUICK/CDS ($\kappa = 0.9$ in Eqn. (10)) can be found in Angerbauer and Rung (2020); Pache (2023). Therein, the method is validated in particular against experimental wind tunnel tests, which underlines its fundamental suitability for providing high-fidelity reference data for the simulation strategy pursued in this paper. An instantaneous impression of the scale-resolving simulations is shown in Fig. 17 based on vortex structures colored with the vorticity magnitude.

In addition to the IDDES studies, further Unsteady RANS (URANS) studies in line with the 2003 version of Menter's SST model are also conducted, see Menter et al. (2003). Results of both viscous methods largely align, which is why only the IDDES simulations are used as a reference and the URANS simulations only classify the numerical effort at this section's end.

Based on the two-dimensional cylinder study from Section 3.1, an impression of the rudimentary behavior of the dynamic circulation adjustment procedure is first given. For this purpose, Fig. 18 shows the development of the ratio of target to the actual rotor circulation from Alg. 4 (left), the longitudinal (center), and the lateral (right) wind coefficient for a TWA of 90 degrees approaching from starboard, evaluated on the second grid level. Three different convection schemes are considered: a UDS (solid black), a TVD-QUICK (orange dotted), and a TVD-CDS (blue dashed) procedure. Again, the volume force is initially undersized and needs to be increased. The discrete adjustment scenarios can be identified in the diagram by the discrete markers every $T = 100$ time steps and again converge quickly to the desired unit value within approximately 10 adjustments. The resulting forces acting on the superstructure are subject to solid fluctuations, even for nearly constant circulation ratios and, thus, volume forces. The fluctuations are significantly reduced for the UDS simulations. However, all three convection schemes result in similar forces averaged over the last 1050 time steps, which are indicated as

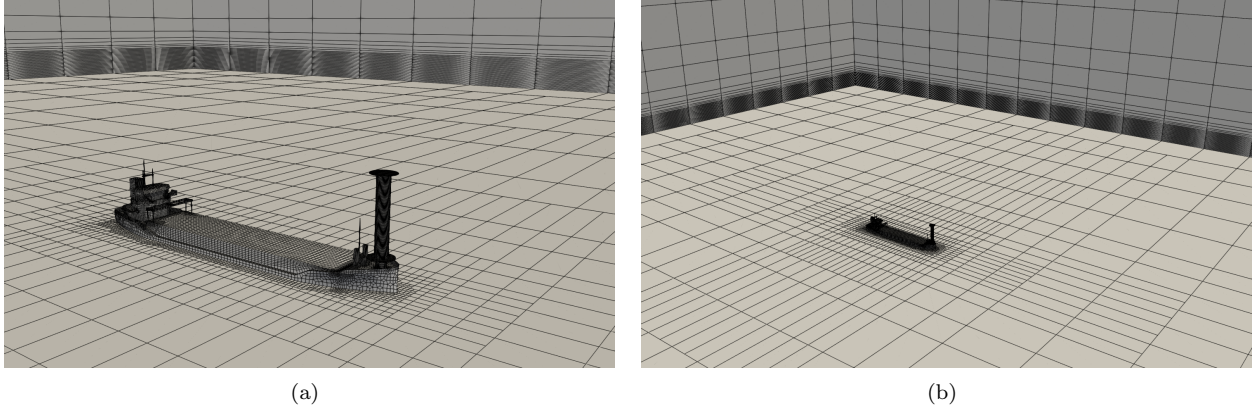


Figure 16: General cargo ship flow: Perspective view of the numerical (a) near and (b) far-field grid.

horizontal lines. Predictions between UDS and TVD-QUICK are close to each other for the longitudinal forces; in the case of the lateral forces, a similarity between UDS and TVD-CDS occurs, which, e.g., underlines the increased lift predictions for TVD-QUICK compared to UDS or TVD-CDS, cf. Fig. 4.

The exemplary study is continued for half the wind polar diagram, i.e., the wind spectrum $0^\circ \leq \text{TWA} \leq 180^\circ$, sampled in 15-degree steps, resulting in 13 simulations to consider the wind spectrum. First, the three introduced numerical grids with different rotor discretization are considered using the flux-blending method with UDS ($\beta = 1.0$) and the hybrid RANS/LES method, resulting in $13 \times 4 = 52$ simulations. Figure 19 displays the longitudinal (left, $C_x = 2f_1/(\rho V^2 A_f)$) and lateral (center, $C_y = 2f_1/(\rho V^2 A_l)$) wind coefficients over the TWA, where A_f and A_l refer to the projected frontal and lateral reference area, respectively. Furthermore, the relative error in the longitudinal forces between the inviscid and the IDDES analyses is shown on the right. Generally, the Eulerian and IDDES predictions have a solid qualitative agreement. Only the results based on the coarsest grid significantly underperform, leading to errors on $\mathcal{O}(10^2\%)$. The differences are particularly pronounced in $90^\circ \leq \text{TWA} \leq 180$ for the longitudinal force and $0^\circ \leq \text{TWA} \leq 120^\circ$ as well as $160^\circ \leq \text{TWA} \leq 180^\circ$ for the lateral companion, i.e., precisely the ranges where the rotor generates a force in the respective direction. Predictions based on the medium and fine grids exhibit comparatively consistent errors of around $\mathcal{O}(10^1\%)$.

The deficiency of the coarse-grid procedure in predicting lift as a function of the TWA is already noticeable in Fig. 19. However, it will be further confirmed below by employing the apparent wind scenario. For this purpose, the wind force coefficients are projected into the apparent wind direction, and the resulting wind parallel and wind orthogonal components are displayed in Fig. 20 on the left and in the center, respectively. The predictions of the cross-wind forces of the coarsest grid deviate significantly from the forces on the finer grids and the IDDES reference results, underscoring the importance of sufficient rotor refinement for adequately predicting lift effects. In addition, the relative errors of the wind-orthogonal forces between the inviscid and inviscid investigations are shown in the right part of the figure. While the two finer grids again lead to errors of $\mathcal{O}(10^1\%)$, the coarsest grid errors tend to be one magnitude higher.

The following investigations are conducted exclusively on the finest grid. In addition to the three considered convection schemes already outlined in Fig. 18, a flux-blending method with 20/80 percent UD/CD is added to the analysis. The four different numerical strategies are re-investigated for all 13 wind scenarios, resulting in

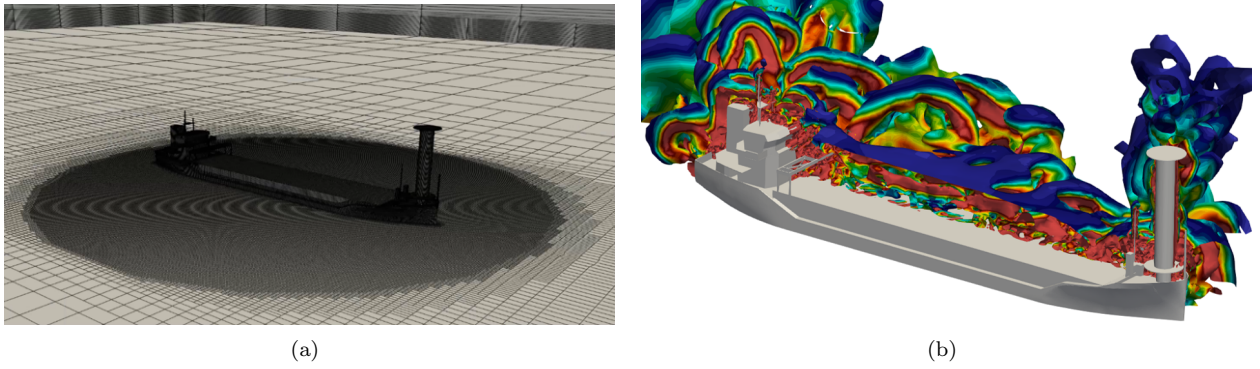


Figure 17: General cargo ship flow: Perspective view of the near-field grid and (b) instantaneous vortex structures colored with the vorticity magnitude of a hybrid averaged/filtered RANS/LES reference simulation at $Re_L = 1 \cdot 10^8$ and $Re_D = 3.45 \cdot 10^6$.

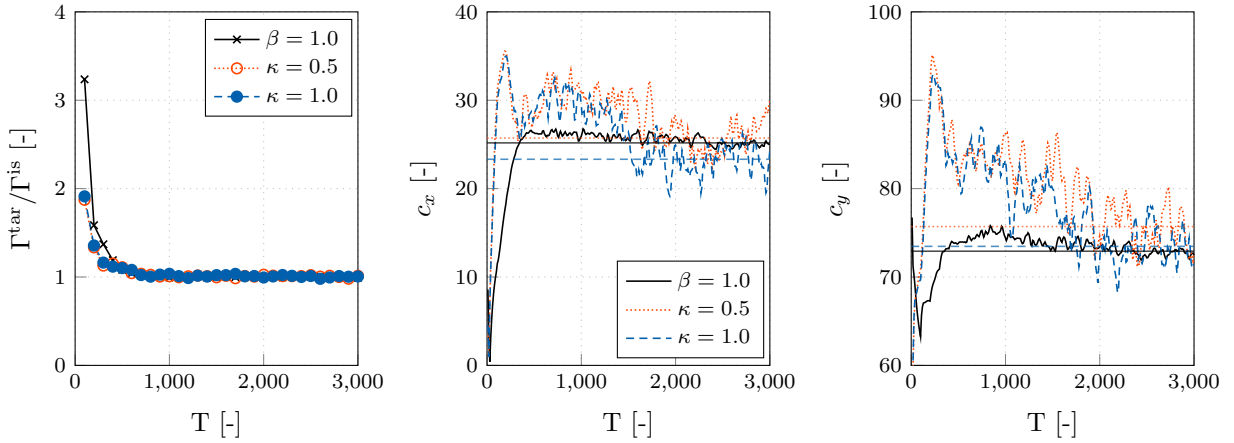


Figure 18: General cargo ship flow : Exemplary development of (left) the ratio of the target/actual flow circulation, (center) the resistance, and (right) the side force coefficient over the simulated time steps for three different treatments of the convective momentum transport at a true wind angle of 90° . Horizontal lines indicate the average resistance values obtained from averaging over the last 1050 time steps.

13x3=39 additional Eulerian simulations. The results are presented in Figs. 21 and 22, and the presentation aligns with the true and apparent wind scenarios in Figures 19-20. The longitudinal or drag force components are again shown on the left, the lateral or side force components in the middle, and error measures on the right. It can be noted that the prediction differences are more minor than those in the previous coarse-grid UD studies. Although all lateral forces in Fig. 2 broadly overestimate the IDDES reference results, they generally follow the

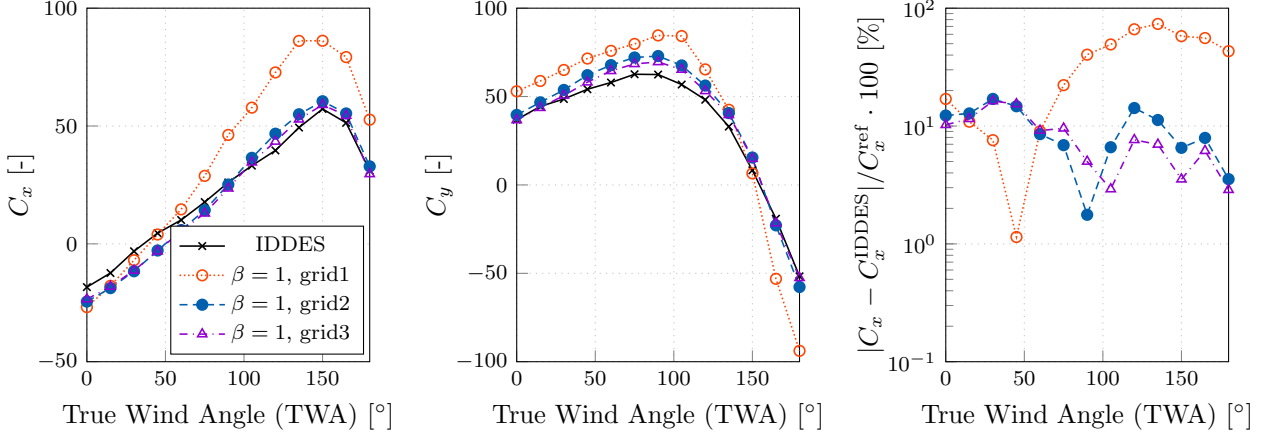


Figure 19: General cargo ship flow: Longitudinal (left) and lateral (center) wind coefficient, as well as the relative longitudinal wind coefficient error (right) over the True Wind Angle for the reference viscous IDDES, as well as three Eulerian studies with differently sized numerical grids.

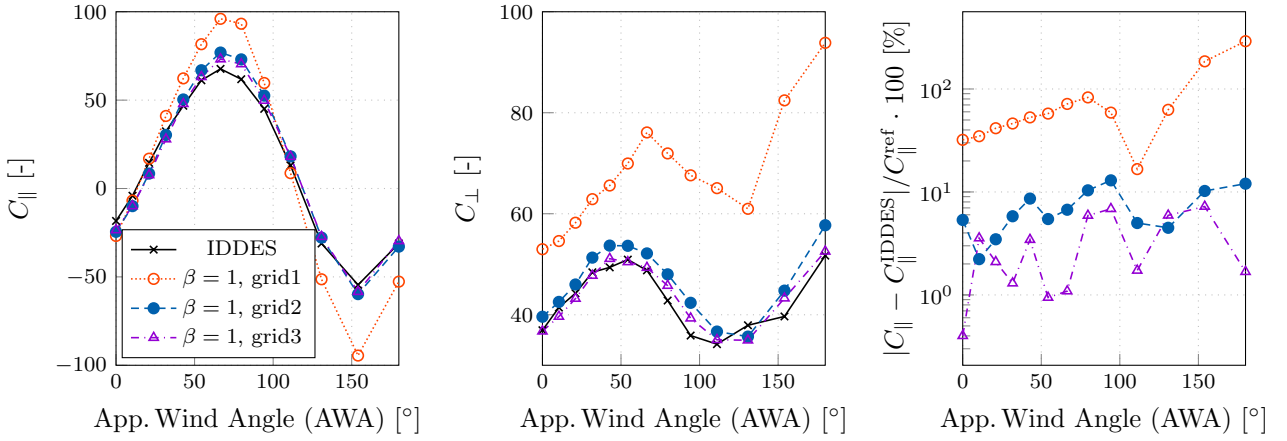


Figure 20: General cargo ship flow: Wind parallel drag (left) and wind orthogonal side (center) force coefficient, as well as the relative cross-wind coefficient error (right) over the Apparent Wind Angle for the reference viscous IDDES, as well as three Eulerian studies with differently sized numerical grids.

qualitative curve. A similar picture appears for the longitudinal forces, which only deviate qualitatively from the reference results for larger TWA and the TVD method, resulting in errors in the range of 20 percent. The apparent wind scenario in Fig. 22 shows that the differences again originate from lift effects, which are still close to, but slightly out of phase with, the reference results for the flux-blending methods but deviate from the IDDES predictions in the case of the TVD-based methods, leading to significantly inflated lift predictions.

Finally, a rough comparison of the numerical effort is conducted. For this purpose, Tab. 1 lists basic discretization as well as averaged, measured simulation data of all three simulation methods used. In addition to the spatial ($\#n_{\text{Cells}}$) and temporal ($\#n_{\text{TimeSteps}}$) discretization count, the table also provides the degree of spatial parallelization in line with a domain decomposition strategy (Kühl et al. (2024)) distributed across processes ($\#n_{\text{CPU}}$) and the required wall clock time \bar{t}^{sim} . The latter values correspond to averaged values from selected previous studies. A combination of process count and averaged simulation wall clock time allows for the estimation of the numerical effort in terms of CPU core hours, i.e., $\text{CPUh} = n_{\text{CPU}}(\bar{t}^{\text{sim}}/3600)$. Although the URANS method is investigated with the same spatial but approximately ten times coarser temporal discretization, the numerical effort is only approximately one-third as high as the IDDES effort, attributable, e.g., to increased iterative effort per time step due to the increased modeling effort.

The numerical effort of the Eulerian methods is reduced by around three orders compared to that of the viscous methods. Regardless of whether the viscous simulations could operate on optimized, coarsened grids

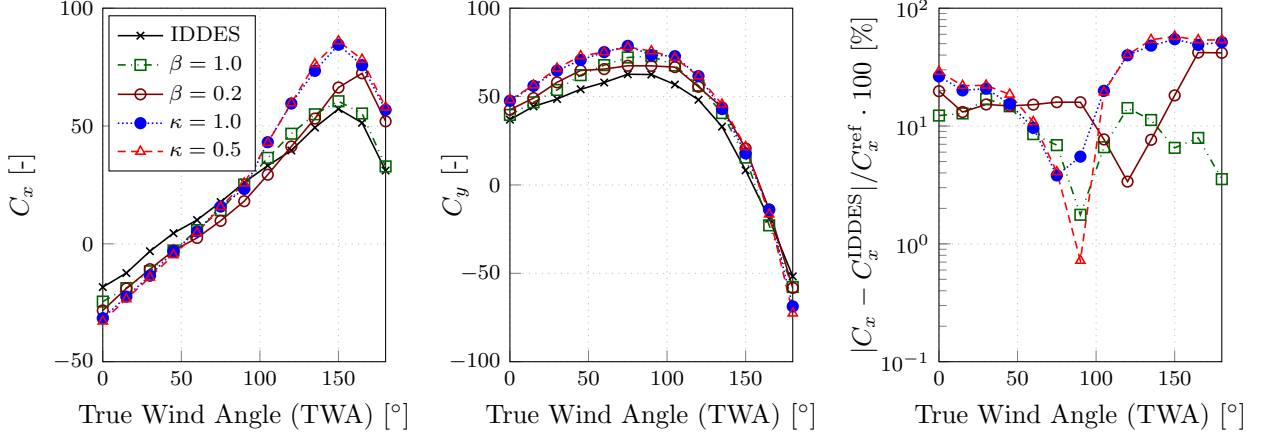


Figure 21: General cargo ship flow: Longitudinal (left) and lateral (center) wind coefficient, as well as the relative longitudinal wind coefficient error (right) over the True Wind Angle for the reference viscous IDDES, as well as four Eulerian studies with different approximations of the convective momentum transport.

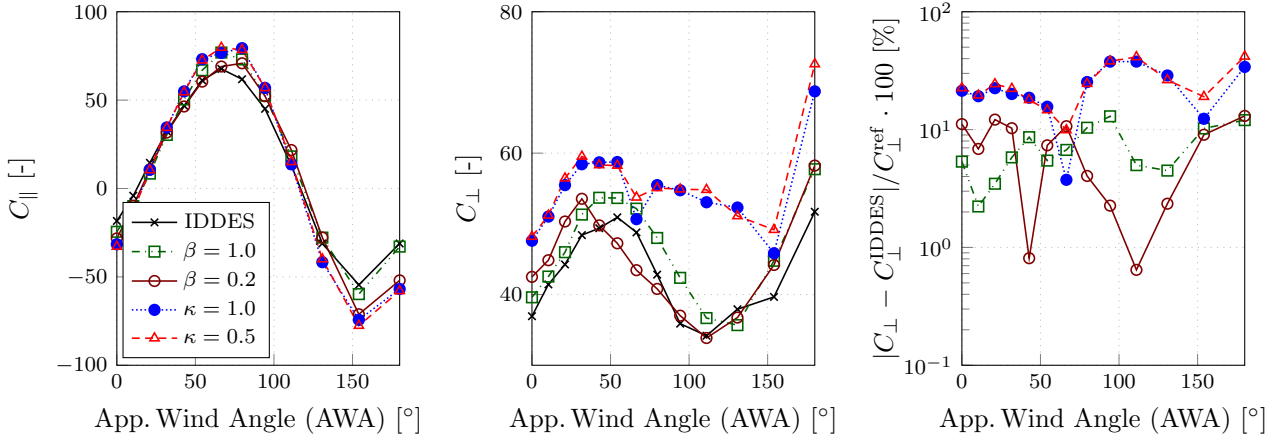


Figure 22: General cargo ship flow: Wind parallel drag (left) and wind orthogonal side (center) force coefficient, as well as the relative cross-wind coefficient error (right) over the Apparent Wind Angle for the reference viscous IDDES, as well as three Eulerian studies with different approximations of the convective momentum transport.

Table 1: General cargo ship flow: Discretization and simulation data of all three utilized simulation methods as well as resulting, required numerical effort.

approach	nCells [-]	nTimeSteps [-]	nCPU [-]	\bar{t}^{sim} [s]	CPUh [-]
IDDES	11 144 780	90 000	256	0.503×10^6	35 769
URANS	11 144 780	9000	256	0.191×10^6	13 596
Eulerian	994 746	3000	96	0.871×10^3	23

with improved time stepping and shorter simulation times, there would still be a significant saving on in the numerical effort, with a simultaneous degeneration of $\mathcal{O}(10^1\%)$ percent in prediction quality.

5 Conclusion & Outlook

The paper presented a frictionless Computational Fluid Dynamics (CFD) method for the rapid aerodynamic estimation of the performance of Flettner rotor installations on ships. The numerical method is based on the inviscid Eulerian flow equations, approximated by a state-of-the-art finite volume method, where a suitable momentum source in regions close to the rotor imposes the rotor circulation. The volume force is adjusted at simulation runtime, i.e., the current rotor circulation is measured, and the volume force is adjusted so that the a priori known rotor circulation is finally achieved. The process is controlled solely via a user-coding interface for momentum source manipulation. It is, therefore, almost entirely externalizable as long as the numerical process has a user interface, which is usually the case with modern CFD solutions.

The neglect of the near-wall discretization refinement and less strict time step requirements result in significantly reduced simulation efforts compared to viscous investigations. This makes the method particularly attractive in an early design phase, for example, for design space exploration. The paper’s applications addressed aerodynamic investigations on large-scale ships at typical Reynolds numbers in the range of $\mathcal{O}(10^8)$, which justifies using a frictionless method to a certain extent. Naturally, parasitic drag can only be inadequately represented with the method, but the paper’s investigations show that the lift-induced companion can be adequately predicted.

The method was benchmarked against a two-dimensional potential flow around a rotating circular cylinder at different spinning ratios. The theoretical results were confirmed for numerical investigations with minimized numerical apparent viscosity, such as utilizing a second-order Central Difference Scheme (CDS) for approximating convective flows. As soon as the numerical method includes a solid amount of numerical viscosity, such as falling back to first-order Upwind Differencing Schemes (UDS), the predicted lift collapses, and the resistance increases slightly.

The flow around a real Flettner rotor was then investigated in an idealized wind tunnel for various spinning ratios. The three-dimensional view also allows the analysis of lift-induced drag. In addition to the inviscid analyses, viscous reference results were generated using the Improved Delayed Detached Eddy Simulation (IDDES) approach at $\text{Re}_D = 2 \cdot 10^6$. Analogous to the two-dimensional investigation, the lift increases for methods with little numerical viscosity. However, this translates into the induced resistance so that the results of the inviscid investigations with decreased [increased] numerical viscosity tend to be further [less far] away from the viscous reference results.

Finally, the method was applied to a general cargo ship with constant speed and $\text{Re}_L = 1 \cdot 10^8$ for variable wind angles. Again, the low-order convection methods are closer to viscous reference results than high-order convection tests. The differences between inviscid and viscous investigations are approximately 10 percent, whereby the numerical effort is reduced by several orders of magnitude, and, with sufficient parallelization, response times are in the range of minutes rather than hours/days.

Future studies should investigate the method further regarding rotor-rotor interaction and generally optimize the algorithmic’s computational efficiency. In addition, the method should be enhanced with ideas for automatic optimal rotor speed determination. Furthermore, adjoint information to support geometric and topological design improvements would be desirable, ideally in a robust form, considering various operating points.

6 Acknowledgments

The current work is part of the ”Development of a Comprehensive Methodology for the Integration of Flettner Rotors on Different Ship Types” research project, which is funded by the German Federal Ministry for Economics and Climate Action (Grant No. 03SX581G). The authors gratefully acknowledge this support.

Declaration of Competing Interest

The authors declare that they have no known competing financial interests or personal relationships that could have appeared to influence the work reported in this paper.

References

R. Angerbauer and T. Rung. Hybrid RANS/LES Simulations of Aerodynamic Flows Around Superstructures of Ships. In *17th Symposium on Hybrid RANS-LES Methods, 17–19 September, 2018, Berlin, Germany*, pages 367–377. Springer, 2020. doi:10.1007/978-3-030-27607-2_30.

- I.S. Arief, A. Santoso, and A. Azzam. Design of Flettner Rotor in Container Carrier 4000 DWT with CFD. International Journal of Marine Engineering Innovation and Research, 2(2):133–139, 2018. doi:10.12962%2Fj25481479.v2i2.2736.
- S. Balay, S. Abhyankar, M.F. Adams, J. Brown, P. Brune, K. Buschelman, L. Dalcin, A. Dener, V. Eijkhout, W.D. Gropp, D. Karpeyev, D. Kaushik, M.G. Knepley, D.A. May, L.C. McInnes, R.T. Mills, T. Munson, K. Rupp, Sanan. P., B.F. Smith, S. Zampini, H. Zhang, and H. Zhang. PETSc Web page. <https://www.mcs.anl.gov/petsc>, 2019. URL <https://www.mcs.anl.gov/petsc>.
- G. Bordogna. Aerodynamics of Wind-Assisted Ships: Interaction Effects on the Aerodynamic Performance of Multiple Wind-pPropulsion Systems. 2020.
- International Towing Tank Conference. Guideline on the CFD-based Determination of Wind Resistance Coefficients. Technical report, ITTC – Recommended Procedures and Guidelines, 2021.
- A. De Marco, S. Mancini, and C. Pensa. Preliminary Analysis for Marine Application of Flettner Rotors. In Proceedings of the 2nd International Symposium on Naval Architecture and Maritime, Istanbul, Turkey, pages 23–24, 2014. doi:10.13140/2.1.4921.3765.
- A. De Marco, S. Mancini, .C Pensa, R. Scognamiglio, and L. Vittiello. Marine Application of Flettner Rotors: Aumerical Study on a Systematic Variation of Geometric Factor by DOE Approach. In MARINE VI: proceedings of the VI International Conference on Computational Methods in Marine Engineering, pages 579–590. CIMNE, 2015.
- J.H. Ferziger and M. Peric. Computational Methods for Fluid Dynamics. Springer Science & Business Media, 2012.
- H.P. Greenspan. The Theory of Rotating Fluids. Cambridge University Press, 1969.
- M.S. Gritskevich, A.V. Garbaruk, J. Schütze, and F.R. Menter. Development of DDES and IDDES Formulations for the $k\text{-}\omega$ Shear Stress Transport Model. Flow, Turbulence and Combustion, 88(3):431–449, 2012. doi:10.1007/s10494-011-9378-4.
- L. Huang, Q. Song, R. Zhang, K. Wang, and R. Ma. Study of the Influence of Rotor Shape on the Aerodynamic Characteristics of Flettner Rotor. In Advances in Machinery, Materials Science and Engineering Application IX, pages 798–804. IOS Press, 2023. doi:10.3233/ATDE230543.
- D. John and J.R. Anderson. Computational Fluid Dynamics: The Basics with Applications. 1995.
- N. Kühn. Adjoint-Based Shape Optimization Constraint by Turbulent Two-Phase Navier-Stokes Systems. PhD thesis, Hamburg University of Technology, 2021.
- N. Kühn. Incremental Singular Value Decomposition Based Model Order Reduction of Scale Resolving Fluid Dynamic Simulations. Computers & Fluids, 291:106579, 2025. doi:10.1016/j.compfluid.2025.106579.
- N. Kühn and T. Rung. Discrete Adjoint Momentum-Weighted Interpolation Strategies. Journal of Computational Physics, 467:111474, 2022. doi:10.1016/j.jcp.2022.111474.
- N. Kühn, P. M. Müller, and T. Rung. Adjoint Complement to the Universal Momentum Law of the Wall. Flow, Turbulence and Combustion, 2021a. doi:10.1007/s10494-021-00286-7.
- N. Kühn, P.M. Müller, and T. Rung. Continuous Adjoint Complement to the Blasius Equation. Physics of Fluids, 33(3):033608, 2021b. doi:10.1063/5.0037779.
- N. Kühn, T. T. Nguyen, M. Palm, D. Jürgens, and T. Rung. Adjoint Node-Based Shape Optimization of Free Floating Vessels. Structural and Multidisciplinary Optimization, 65:247, 2022. doi:10.1007/s00158-022-03338-2.
- N. Kühn, H. Fischer, M. Hinze, and T. Rung. An Incremental Singular Value Decomposition Approach for Large-Scale Spatially Parallel & Distributed but Temporally Serial Data – Applied to Technical Flows. Computer Physics Communications, 296:109022, 2024. doi:10.1016/j.cpc.2023.109022.

- C.S. Kwon, S.M. Yeon, Y.C. Kim, Y.G. Kim, Y.H. Kim, and H.J. Kang. A Parametric Study for a Flettner Rotor in Standalone Condition Using CFD. International Journal of Naval Architecture and Ocean Engineering, 14:100493, 2022. doi:10.1016/j.ijnaoe.2022.100493.
- M. Loft, N. Kühn, M.P. Buckley, J.R. Carpenter, M. Hinze, F. Veron, and T. Rung. Two-phase Flow Simulations of Surface Waves in Wind-Forced Conditions. Physics of Fluids, 35(7), 2023. doi:10.1063/5.0156963.
- M. Manzke. Development of a Scalable Method for the Efficient Simulation of Flows using Dynamic Goal-Orientated Local Grid-Adaption. PhD thesis, Hamburg University of Technology, 2018.
- F.R. Menter. Two-Equation Eddy-Viscosity Turbulence Models for Engineering Applications. AIAA Journal, 32(8):1598–1605, 1994. doi:10.2514/3.12149.
- F.R. Menter. Review of The Shear-Stress Transport Turbulence Model: Experience From an Industrial Perspective. International Journal of Computational Fluid Dynamics, 23(4):305–316, 2009. doi:10.1080/10618560902773387.
- F.R. Menter, M. Kuntz, and R. Langtry. Ten Years of Industrial Experience with the SST Turbulence Model. Turbulence, Heat and Mass Transfer, 4(1):625–632, 2003.
- P. M. Müller, N. Kühn, M. Siebenborn, K. Deckelnick, M. Hinze, and T. Rung. A Novel p -Harmonic Descent Approach Applied to Fluid Dynamic Shape Optimization. Structural and Multidisciplinary Optimization, 2021. doi:10.1007/s00158-021-03030-x.
- R. Pache. Datenbasierte Modellierung der Aerodynamischen Lasten auf Überwasserschiffe. PhD thesis, Hamburg University of Technology, 2023.
- R. Pache and T. Rung. Data-Driven Surrogate Modeling of Aerodynamic Forces on the Superstructure of Container Vessels. Engineering Applications of Computational Fluid Mechanics, 16(1):746–763, 2022. doi:10.1080/19942060.2022.2044383.
- L. Radtke, G. Bletsos, N. Kühn, T. Suchan, T. Rung, A. Düster, and K. Welker. Parameter-Free Shape Optimization: Various Shape Updates for Engineering Applications. Aerospace, 10(9), 2023. doi:10.3390/aerospace10090751.
- T. Rung, K. Wöckner, M. Manzke, J. Brunswig, C. Ulrich, and A. Stück. Challenges and Perspectives for Maritime CFD Applications. Jahrbuch der Schiffbautechnischen Gesellschaft, 103:127–39, 2009.
- J.A. Samareh. Status and Future of Geometry Modeling and Grid Generation for Design and Optimization. Journal of Aircraft, 36(1):97–104, 1999. doi:10.2514/2.2417.
- J. Seifert. A review of the Magnus Effect in Aeronautics. Progress in Aerospace Sciences, 55:17–45, 2012. doi:10.1016/j.paerosci.2012.07.001.
- P.R. Spalart, W.H. Jou, M. Strelets, and S.R. Allmaras. Comments on the Feasibility of LES for Wings and on the Hybrid RANS/LES Approach. In Proceedings of the First AFOSR International Conference on DNS/LES, 1997, pages 137–147, 1997.
- A. Stück. Adjoint Navier-Stokes Methods for Hydrodynamic Shape Optimisation. PhD thesis, Hamburg University of Technology, 2012.
- B. Van Leer. Towards the Ultimate Conservative Difference Scheme. v. a Second-Order Sequel to Godunov’s Method. Journal of Computational Physics, 32(1):101–136, 1979. doi:10.1016/0021-9991(79)90145-1.